Using a Speed-Dependent Voigt Line Shape to Retrieve O_2 from Total Carbon Column Observing Network Solar Spectra to Improve Measurements of XCO_2 ~~Improving the Retrieval of XCO_2 from Total Carbon Column Network Solar Spectra~~

Authors: Joseph Mendonca[1], Kimberly Strong[1], Debra Wunch[1], Geoffrey C. Toon[2], David A. Long[3], Joseph T. Hodges[3], Vincent T. Sironneau[3], and Jonathan E. Franklin[4].

1. Department of Physics, University of Toronto, Toronto, ON, Canada

2. Jet Propulsion Laboratory, Pasadena, CA, USA

3. National Institute of Standards and Technology, Gaithersburg, MD, USA

4. Harvard John A. Paulson School of Engineering and Applied Sciences, Cambridge, MA, USA

Correspondence to: Joseph Mendonca (joseph.mendonca@utoronto.ca)

Abstract. High-resolution, laboratory, absorption spectra of the $a^1\Delta_g \leftarrow X^3\Sigma_g^-$ oxygen(O_2) band measured using cavity ring-down spectroscopy were fitted using the Voigt and speed-dependent Voigt line shapes. We found that the speed-dependent Voigt line shape was better able to model the measured absorption coefficients than the Voigt line shape. We used these line shape models to calculate absorption coefficients to retrieve atmospheric ~~T~~total columns abundances of O_2 ~~were retrieved~~ from ground-based ~~high resolution absorption~~ spectra from four Fourier transform spectrometers that are apart of the Total Carbon Column Observing Network (TCCON) ~~sites using both Voigt and speed-dependent Voigt line shapes to calculate absorption coefficients. A l~~Lower O_2 ~~concentration~~ total columns ~~was~~ were retrieved with the speed-dependent Voigt line shape, ~~with~~ and the difference between the total columns retrieved using the Voigt and speed-dependent Voigt line shapes ~~increasing~~ increased as a function of solar zenith angle. Previous work has shown that carbon dioxide (CO_2) total columns ~~were also retrieved from the same spectra using a Voigt line shape and~~ are better retrieved using a speed-dependent Voigt line shape with line mixing. The column-averaged dry-air mole fraction of CO_2 (XCO_2) was calculated using the ratio between the columns of CO_2 and O_2 ~~columns~~ retrieved (from the same spectra) with both line shapes from measurements made over a one-year period at the four sites. ~~and compared.~~ The inclusion of speed dependence in the O_2 retrievals significantly reduces the airmass dependence of XCO_2. ~~The TCCON empirical airmass correction factor for XCO_2 derived from a year of measurements from TCCON sites at Darwin, Lamont, and Park Falls for XCO_2 improved from 0.0071±0.0057 to 0.0012±0.0054 when speed dependence was included. XCO_2 retrieved with the Voigt and speed-dependent Voigt line shapes was compared to aircraft profiles measured at 13 TCCON sites. T~~ and the bias between the TCCON measurements and ~~the~~ calibrated integrated aircraft profile measurements was reduced from ~~0.9897±0.0005~~ 1% to ~~1.0041±0.0005~~ 0.4%. ~~for XCO_2 retrieved with the Voigt and speed-dependent Voigt line shapes respectively.~~ These results suggest that speed dependence should be included in the forward model when fitting near-infrared CO_2 and O_2 spectra to improve the accuracy of XCO_2 measurements.

1. Introduction

Accurate remote sensing of greenhouse gases (GHGs), such as CO_2, in Earth's atmosphere is important for studying the carbon cycle ~~in order~~ to better understand and predict climate change. The absorption of solar radiation by O_2 in the Earth's atmosphere is important because it can be used to study the properties of clouds and aerosols, and to determine vertical profiles of temperature and surface pressure. Wallace and Livingston (1990) were the first to retrieve total columns of O_2 from some of the discrete lines of the $a^1\Delta_g \leftarrow X^3\Sigma_g^-$ band of O_2 centered at 1.27 μm (which will be referred to bellow as the 1.27 μm band) using atmospheric solar absorption spectra from the Kitt Peak observatory. Mlawer et al. (1998) recorded solar absorption spectra in the near-infrared (NIR) region to study collision-induced absorption (CIA) in the $a^1\Delta_g \leftarrow X^3\Sigma_g^-$ band ~~of O_2 centered at 1.27 μm (which will be referred to as the 1.27 μm band)~~ as well as two other O_2 bands. The spectra were compared to a line-by-line radiative transfer model and the differences between the measured and calculated spectra showed the need for better absorption coefficients in order to accurately model the 1.27 μm band (Mlawer et al., 1998). Subsequently, spectroscopic parameters needed to calculate the absorption coefficients from discrete transitions of the 1.27 μm band were measured in multiple studies (Cheah et al., 2000; Newman et al., 1999, 2000; Smith and Newnham, 2000), as was collision-induced absorption (CIA) (Maté et al., 1999; Smith and Newnham, 2000), while Smith et al. (2001) validated the work done in Smith and Newnham (2000) using solar absorption spectra.

The 1.27 μm band is of particular importance to the Total Carbon Column Observing Network (TCCON) (Wunch et al., 2011). TCCON is a ground-based remote sensing network that makes accurate and precise measurements of GHGs for satellite validation and carbon cycle studies. Using the O_2 column retrieved from solar absorption spectra, the column-averaged dry-air mole fraction of CO_2 (XCO_2) has been shown to provide better precision than using the surface pressure to calculate XCO_2 (Yang et al., 2002) ~~(Washenfelder et al., 2006)~~. The O_2 column is retrieved from the 1.27 μm band because of its close proximity to the spectral lines used to retrieve CO_2, thereby reducing the impact of solar tracker mis-pointing and an imperfect instrument line shape (ILS) (Washenfelder et al., 2006). To improve the retrievals of O_2 from the 1.27 μm band, Washenfelder et al. (2006) found that adjusting the spectroscopic parameters in HITRAN 2004 (Rothman et al., 2005) decreased the airmass and temperature dependence of the O_2 column. These revised spectroscopic parameters were included in HITRAN 2008 (Rothman et al., 2009). Atmospheric solar absorption measurements from this band made at the Park Falls TCCON site by Washenfelder et al. (2006) were the first measurements to observe the electric-quadrupole transitions (Gordon et al., 2010). Leshchishina et al. (2011, 2010) subsequently used cavity-ring-down spectra to retrieve spectroscopic parameters for the 1.27 μm band using a Voigt spectral line shape and these parameters were included in HITRAN 2012 (Rothman et al., 2013). Spectroscopic parameters for the discrete spectral lines of the O_2 1.27 μm band from HITRAN 2016 (Gordon et al., 2017) are very similar to HITRAN 2012 except that HITRAN2016 includes improved line positions reported by Yu et al. (2014).

Extensive spectral line shape studies have been performed for the O_2 A-band, which is centered at 762 nm and used by the Greenhouse Gases Observing Satellite (GOSAT) (Yokota et al., 2009) and the Orbiting Carbon ~~Observing~~

Observatory-2 (OCO-2) satellite (Crisp et al., 2004) to determine surface pressure. ~~These studies~~ Studies have ~~showed~~ shown that the Voigt line shape ~~was~~ is inadequate to describe the spectral line shape of the discrete O_2 lines in the A-band~~;~~. Dicke narrowing occurs when the motion of the molecule is diffusive due to collisions changing the velocity and direction of the molecule during the time that it is excited. This diffusive motion is taken into account by averaging over many different Doppler states resulting in a line width that is narrower than the Doppler width (Dicke, 1953). ~~The need to take into account Dicke narrowing was shown in~~ Long et al. (2010) and Predoi-Cross et al. (2008) found it necessary to use a spectral Line shape model that accounted for Dicke narrowing when fitting the discrete lines of the O_2 A-band. ~~and~~ Line mixing, which occurs when collisions transfer intensity from one part of the spectral band to another (Lévy et al., 1992), was shown to be prevalent in multiple studies (Predoi-Cross et al., 2008; Tran et al., 2006; Tran and Hartmann, 2008). Tran and Hartmann (2008) showed that including line mixing when calculating the O_2 A-band absorption coefficients reduced the airmass dependence of the O_2 column retrieved from TCCON spectra. When fitting cavity ring-down spectra of the O_2 A-band, Drouin et al. (2017) found it necessary to use a speed-dependence Voigt line shape, which takes into account different speeds at the time of collision (Shannon et al., 1986), with line mixing to properly fit the discrete spectral lines of the O_2 A-band.

The need to include non-Voigt effects when calculating absorption coefficients for the O_2 1.27 μm band was first shown in Hartmann et al. (2013) and Lamouroux et al. (2014). In Hartmann et al. (2013) and Lamouroux et al. (2014), Lorentzian widths were calculated using the re-quantized classical molecular-dynamics simulations (rCMDSs) and used to fit cavity-ring-down spectra with a Voigt line shape for some isolated transitions in the O_2 1.27 μm band. The studies concluded that a Voigt line shape is insufficient for modeling the spectral lines of the O_2 1.27 μm band and that effects such as speed dependence and Dicke narrowing should be included in the line shape calculation.

In this study, air-broadened laboratory cavity-ring-down spectra of the O_2 1.27 μm band were fitted using a spectral line shape that takes into account speed dependence. The ~~corresponding~~ derived spectroscopic parameters for the speed-dependent Voigt line shape were used to calculate absorption coefficients when fitting high-resolution solar absorption spectra. Using these new O_2 total columns, and the simultaneously measured ~~were combined with~~ CO_2 total columns, ~~from~~ using the updated line shape model described by Mendonca et al. (2016), to calculate XCO_2 and compared these results with XCO_2 retrieved using a Voigt line shape. Section 2 details the formulas used to calculate absorption coefficients using different spectral line shapes. In Section 3, we describe the retrieval of spectroscopic parameters from three air-broadened cavity-ring-down spectra fitted with a speed-dependent Voigt line shape. For Section 4, the speed-dependent line shape along with the retrieved spectroscopic parameters is used to fit solar absorption spectra from four TCCON sites and retrieve total columns of O_2, which is compared to O_2 retrieved using a Voigt line shape. In Section 5, we investigate the change in the airmass dependence of XCO_2 with the new O_2 ~~parameters~~ retrievals. In Section 6, we discuss our results and their implications for remote sensing of greenhouse gases.

2. Absorption Coefficient Calculations

2.1 Voigt Line Shape

The Voigt line shape is the convolution of the Lorentz and the Gaussian ~~Doppler line shapes~~ profiles, which model pressure and Doppler broadening of the spectral line respectively. The corresponding absorption coefficient, k, at a given wavenumber v becomes :

$$k(v) = N \sum_j S_j \left(\frac{1}{\gamma_{D_j}}\right)\left(\frac{\ln(2)}{\pi}\right)^{1/2} \left(Re\left[c(v, x_j, y_j)\right]\right) \quad (1)$$

where N is the number density, S_j is the line intensity of spectral line j, γ_{D_j} is the Doppler half-width (HWHM), c is the complex error function, and

$$x_j = \frac{\left(v - v_j^o - P\delta_j^o\right)}{\gamma_{D_j}} (\ln(2))^{1/2}, \; y_j = \frac{\gamma_{L_j}}{\gamma_{D_j}} (\ln(2))^{1/2} . \quad (2)$$

Here, v_j^o is the position of the spectral line j, P is the pressure, and δ_j^o is the pressure-shift coefficient. The Lorentz half-width, γ_{L_j}, is calculated using:

$$\gamma_{L_j}(T) = \mathrm{P}\, \gamma_{L_j}^o \left(\frac{296}{T}\right)^n \quad (3)$$

where $\gamma_{L_j}^o$ is the air-broadened Lorentz half-width coefficient (at reference temperature 296 K) and n is the exponent of temperature dependence. The Voigt line shape assumes that pressure broadening is accurately represented by a Lorentz profile calculated for the stastical average velocity at the time of collission.

2.2 Speed-Dependent Voigt Line Shape

The speed-dependent Voigt line shape refines the pressure broadening component of the Voigt by calculating multiple Lorentz profiles for different speeds at the time of collision. The final contribution from pressure broadening to the speed-dependent Voigt is the weighted sum of Lorentz profiles (weighted by the Maxwell-Boltzmann speed-distribution) calculated for different speeds at the time of collision. ~~To take speed dependence into account, we use t~~The speed-dependent Voigt line shape (Ciuryło, 1998) with the quadratic representation of the Lorentz width and pressure shift (Rohart et al., 1994) is:

$$k(v) = N\left(\frac{2}{\pi^{\frac{3}{2}}}\right)\sum_j S_j \int_{-\infty}^{\infty} e^{-\mathrm{V}^2} \mathrm{V}\left(tan^{-1}\left[\frac{x_j - B a_{\delta_j}(\cancel{(V)}\mathrm{V}^2 - 1.5) + \mathrm{V}}{y_j(1 + a_{\gamma_{L_j}}(\cancel{(V)}\mathrm{V}^2 - 1.5))}\right]\right) dV \quad (4)$$

where $a_{\gamma_{L_j}}$ is the speed-dependent Lorentz width parameter (unitless) for line j, a_{δ_j} is the speed- dependent pressure-shift parameter (unitless), B is $\frac{(\ln(2))^{1/2}}{\gamma_{D_j}}$, V is the ratio of the absorbing molecule's speed to the most probable speed of the absorbing molecule, and all other variables are defined before.

3. Fitting Laboratory Spectra

O_2, unlike CO_2 and CH_4, cannot produce an electric dipole moment and therefore should not be infrared active. However, O_2 has two unpaired electrons in the ground state that produce a magnetic dipole moment. Due to the unpaired electrons in the ground state ($X^3\Sigma_g^-$) the rotational state (N) is split into three components which are given by $J = N$-1, $J = N$, and $J = N$+1, while in the upper state ($a^1\Delta_g$), $J = N$. When labeling a transition, the following nomenclature is used $\Delta N(N'')\Delta J(J'')$ (Leshchishina et al., 2010), where ΔN is the difference between N' in the upper state and N'' in the lower state, ΔJ is the difference between J' in the upper state and J'' in the lower state. The magnetic transitions of $a^1\Delta_g \leftarrow X^3\Sigma_g^-$ allow for ΔJ=0, ±1. This leads to 9 branches observed: P(N'')Q(J''), R(N'')Q(J''), and Q(N'')Q(J''), for ΔJ=0, O(N'')P(J''), P(N'')P(J''), and Q(N'')P(J''), for ΔJ=-1, and S(N'')R(J''), R(N'')R(J''), and Q(N'')R(J''), for ΔJ=1.

Absorption coefficients for three room temperature air-broadened (NIST Standard reference materal® 2659a containing 79.28 % N_2, 20.720(43) % O_2, 0.0029 % Ar, 0.00015 % H_2O, and 0.001 % other compounds) spectra were measured at the National Institute of Standards and Technology (NIST) using the frequency-stabilized cavity-ring-down spectroscopy (FS-CRDS)) technique (Hodges et al., 2004; Hodges, 2005). The absorption spectra were acquired at pressures of 131 kPa, 99.3 kPa, and 66.9 kPa, at temperatures of 296.28 K, 296.34 K, and 296.30 K respectively. Figure 1a shows the three measured absorption spectra. A more detailed discussion of the present FS-CRDS spectrometer can be found in Lin et al. (2015).

The spectra were fitted individually using a Voigt line shape (Eq. 1), with S_j, $\gamma_{L_j}^o$, and δ_j^o for the main isotope of the magnetic dipole lines of the O_2 1.27 μm band for lines with an intensity greater than 7.0×10^{-28} $cm^{-1}/(molecule\ cm^{-2})$. The spectroscopic parameters measured in Leshchishina et al. (2011) for the spectral lines of interest were used as the a priori for the retrieved spectroscopic parameters. The line positions were left fixed to the values measured in Leshchishina et al. (2011), and all other O_2 spectral lines (intensity less 7.0×10^{-28} $cm^{-1}/(molecule\ cm^{-2})$) were calculated using a Voigt line shape with spectroscopic parameters from HITRAN 2012 (Rothman et al., 2013). Spectral fits were done using the lsqnonlin function in Matlab, with a user-defined Jacobian matrix. The Jacobian was constructed by taking the derivative of the absorption coefficients with respect to the parameters of interest. Using an analytical Jacobian instead of the finite difference method is both computationally faster and more accurate. The Voigt line shape was calculated using the Matlab code created by Abrarov and Quine (2011) to calculate the complex error function and its derivatives. To take collision-induced absorption (CIA) into account, a set of 50 Legendre polynomials were added together by retrieving the weighting coefficients needed to add the polynomials to fit the CIA for each spectrum. Figure 1b shows the residual (measured minus calculated absorption coefficients) when using a Voigt line shape with the retrieved spectroscopic parameters. The plot shows that residual structure still remains for all three spectra. The Root Mean Square (RMS) residual values for the spectra are given by the legend at the side of the plot.

Figure 2 is the same plot as Figure 1 but for the P(11)P(11), P(11)Q(10), P(9)P(9), and P(9)Q(8) spectral lines only. Figure 2b shows that for all four spectral lines there is a “W” shaped residual at the line center. The P(11)P(11) line

was also measured by Hartmann et al. (2013) at pressures ranging from 6.7 to 107 kPa. Figure 5 of Hartmann et al. (2013) shows the P(11)P(11) line at a pressure of 66.7 kPa, which is approximately the pressure of the 66.9 kPa spectrum (blue spectrum in Figure 1 and 2). When one compares the blue residual of the P(11)P(11) line in Figure 2b to that of the residual of the left panel of Figure 5 of Hartmann et al. (2013), one can see that the residuals are the same. Figure 6 of Hartmann et al. (2013) show that the amplitude of the residual increases with decreasing pressure, which is also seen in Figure 2b. Figure 3 of Lamouroux et al. (2014) shows the same "W" residual for the P(9)P(9) lines and that the amplitude of the residual increases with decreasing pressure (although for lower pressures) consistent with the results for the P(9)P(9) line in Figure 2b.

Figure 1c shows the residual when using the speed-dependent Voigt (Eq. 4) to fit each spectrum individually. To use Eq. (4) requires integration over all possible speeds, which is not computationally practical, so we employ the simple numerical integration scheme as was done by Wehr (2005). When fitting the spectra, parameters S_j, $\gamma_{L_j}^o$, δ_j^o, $a_{\gamma_{L_i}}$ and a_{δ_j} were retrieved for lines of intensity greater than $7.0\text{x}10^{-28}$ $\text{cm}^{-1}/(\text{molecule cm}^{-2})$, while all other O_2 lines were calculated using a Voigt line shape and spectroscopic parameters from HITRAN 2012 (Rothman et al., 2013b). The Jacobian matrix was created by taking the derivative with respect to each parameter of interest, as was done with the Voigt fits. By taking speed-dependent effects into account, the residuals were reduced to 25 times smaller than those for the Voigt fit and the RMS residuals (given in the legend of Figure 1c) are 10 times smaller. However, some residual structure still remains, which is more evident in the in the Q and R branches than the P branch. Figure 2c shows the four lines in the P branch, as discussed when analyzing the Voigt fits. A small residual "W" remains at line center, as well as residuals from weak O_2 lines.

Figure 3 shows the averaged intensity, Lorentz width coefficient, pressure shift coefficient, and speed-dependent shift coefficient of the 1.27 μm O_2 band, retrieved from the three spectra, plotted as a function of ~~J''.~~ quantum number m which is m=-J (where J is the lower state rotational quantum number) for the P-branch lines, m=J for the Q-branch lines, and m=J+1 for the R-branch lines. The intensity, Lorentz widths, and pressure shifts show a ~~J''~~ m dependence for these parameters for the P and R sub-branches. The measured Lorentz widths and pressure shifts for the Q sub-branches show a ~~J''~~ m dependence but are not as strong as the P and R sub-branches. This is because the Q branch lines are broadened enough to blend with each other since they are spaced closer together than the P or R branch lines. Figure 1c shows that some of the residual structure in the Q branch increases with pressure and is partly due to the blending of these transitions as the pressure increases. The weak O_2 absorption lines also blend in with the Q branch, contributing to the residual structure in Figure 1c. We tried retrieving the spectroscopic parameters for the weak O_2 absorption lines, but since they were overlapping with the strong O_2 lines, it was not possible. Figure 4a shows the retrieved speed-dependent width parameter averaged over the three spectra, plotted as a function of ~~J''~~ m, showing that it increases with ~~J''~~ m. Error bars correspond to the 2σ standard deviation and are large regardless of sub-branch. Figure 4b shows the retrieved speed-dependent width for the PQ sub-branch for the different pressures. The speed-dependent width shows the same ~~J''~~ m dependence regardless of pressure, but also increases with decreasing pressure as is the case for sub-branches. It should be noted that the speed-dependent width parameter should be independent of pressure.

4. Fitting Solar Spectra

High-resolution solar absorption spectra were measured at four TCCON sites using a Bruker IFS 125HR FTIR spectrometer with a room temperature InGaAs detector at a spectral resolution of 0.02 cm^{-1} (45 cm maximum optical path difference). The raw interferograms recorded by the instrument were processed into spectra using the I2S software package (Wunch, D. et al., 2015) that corrects ~~them for~~ solar intensity variations (Keppel-Aleks et al., 2007), phase errors (Mertz, 1967), and laser sampling errors (Wunch, D. et al., 2015), and then preforms a fast Fourier transform~~s~~ to convert the interferograms into spectra (Bergland, 1969). The GGG software package (Wunch, D. et al., 2015) is used to retrieve total columns of atmospheric trace gases. GFIT is the main code that contains the forward model, which calculates a solar absorption spectrum using a line-by-line radiative transfer model and an iterative non-linear least square fitting algorithm that scales an a priori gas profile to obtain the best fit to the measured spectrum. A priori profiles for GHGs are created by an empirical model in GGG that is based on measurements from the balloon-borne JPL MkIV Fourier Transform Spectrometer (FTS) (Toon, 1991), the Atmospheric Chemistry Experiment (ACE) FTS instrument aboard SCISAT (Bernath et al., 2005), and in situ GLOBALVIEW data (Wunch et al., 2011). Temperature and pressure profiles, as well as H_2O a priori profiles are generated from the National Centers for Environmental Prediction (NCEP) data. The calculations are performed for 71 atmospheric layers (0 km to 70 km), so all a priori profiles are generated on a vertical grid of 1 km.

In the current GGG software package (Wunch, D. et al., 2015), the forward model of GFIT calculates absorption coefficients for the discrete lines of the O_2 1.27 µm band using a Voigt line shape and spectroscopic parameters from Washenfelder et al. (2006a) and Gordon et al. (2010). To take CIA into account, absorption coefficients are calculated using a Voigt line shape and spectroscopic parameters from the foreign-collision-induced absorption (FCIA) and self-collision-induced absorption (SCIA) spectral line lists provided with the GGG software package (Wunch, D. et al., 2015). Spectroscopic parameters in the FCIA and SCIA line lists were retrieved by Geoff Toon by fitting the laboratory spectra of Smith and Newnham (2000). This was done by retrieving the integrated absorption at every 1 cm^{-1} of the spectrum and using a Voigt line shape, with fixed Lorentz width and no pressure shift. In GFIT, a volume scale factor is retrieved for the CIA and discrete lines separately so that the O_2 column is derived from the discrete lines of the 1.27 µm band only. Airglow is not considered when fitting the 1.27 µm band since the spectrometer views the sun directly, and airglow is overwhelmed by such a bright source. The continuum level and tilt of the 100% transmission level is fitted using a weighted combination of the first two Legendre polynomials. Absorption coefficient for all other trace gases are calculated using a Voigt line shape and spectroscopic parameters from the atm.101 line list (Toon, G. C., 2014a)~~(Wunch, D. et al., 2015)~~ and solar lines are fitted using the solar line list (Toon, G. C., 2014b)~~(Wunch, D. et al., 2015)~~.

Figure 5 shows the spectral fit to a solar absorption spectrum recorded at Eureka on March 27, 2015, at a solar zenith angle (SZA) of 81.32° (airmass of 6.3). This spectrum is an average of 5 Eureka scans. The TCCON standard is single scan but 5 scans were averaged to decrease the noise. The measured spectrum (red circles), calculated spectrum (black circles) and transitions from all gases in the window (colored lines, refer to the legend for different gases) are shown in Figure 5b. The residual obtained using a Voigt line shape to calculate the discrete lines of the O_2

1.27 μm band is shown in red in Figure 5a. The blue residual is the result of using a speed-dependent Voigt line shape with the spectroscopic parameters retrieved from fitting the absorption coefficients in Section 3. To decrease the amount of time it takes to calculate the absorption coefficients, the quadratic-Speed Dependent Voigt (qSDV) computational approach of Ngo et al. (2013) and Tran et al. (2013)was used instead of Eq. (4) since it requires the Voigt calculation only twice, while Eq. (4) requires numerical integration scheme with 33 iterations. The temperature-dependent parameter of the Lorentz width of the discrete lines of the O_2 1.27 μm band reported in HITRAN 2012 was used to take temperature dependence into account for $\gamma_{L_j}(T)$. There was only a slight improvement in the fit residuals with the new absorption coefficients (using the qSDV), as seen in Figure 5a. Absorption coefficients calculated with the qSDV were used to retrieve total columns of O_2 from solar spectra recorded over a one year period at TCCON sites in Eureka (eu) (Nunavut, Canada) (Batchelor et al., 2009; Strong et al., 2017)~~(Batchelor et al., 2009)~~, Park Falls (pa) (Wisconsin, U.S.A) (Washenfelder et al., 2006; Wennberg et al., 2017)~~(Washenfelder et al., 2006b)~~, Lamont (oc) (Oklahoma, U.S.A) (Wennberg et al., 2017b), and Darwin (db) (Australia) (Deutscher et al., 2010; Griffith et al., 2017)~~(Deutscher et al., 2010)~~. In total 131 124 spectra were fitted using the qSDV and the average root mean square (RMS) residual of the fit only decreased by 0.5 %.

5. Impact of O_2 Columns on XCO_2 Measurements

The O_2 column retrieved from the 1.27 μm band with a Voigt line shape and spectroscopic parameters from the atm.101 line list (Toon, G. C., 2014a) ~~(Wunch, D. et al., 2015)~~ has an airmass dependence such that the O_2 column retrieved increases as a function of solar zenith angle (or airmass). Using spectra recorded from Eureka, Park Falls, Lamont, and Darwin over one-year periods, total columns of O_2 were retrieved using (1) a Voigt spectral line shape with spectroscopic parameters from the atm.101 line list and (2) the qSDV with the spectroscopic parameters determined in Section 3. Figure 6 shows the percent difference calculated as the column from the qSDV retrieval minus the column from the Voigt retrieval, which was then divided by the latter and multiplied by 100, plotted as a function of solar zenith angle (SZA). At the smallest SZA, the qSDV retrieves 0.75% less O_2 than the Voigt, with the difference increasing to approximately 1.8% as the SZA approaches 90°. Figure 7 shows XAIR from Park Falls on June 18, 2013. XAIR is the column of air (determined using surface pressure recorded at the site) divided by the column of O_2 retrieved from the spectra and multiplied by 0.2095, which is the dry air mole fraction of O_2 in Earth's atmosphere. Ideally XAIR should be 1 but when using O_2 retrieved with a Voigt line shape (red points) it is closer to 0.98 near noon (small SZA) and lower near the start and end of the day (large SZA). When using O_2 retrieved with the qSDV, XAIR is closer to 0.988 near noon and a bit higher near the start and end of the day. This means the O_2 column, retrieved with the qSDV, decreases as a function of SZA, while previously the column increased as a function of SZA when the Voigt line shape is used.

5.1 Airmass Dependence of XCO_2

Since the standard TCCON XCO_2 (and all other XGas) is calculated using the column of O_2 instead of the surface pressure, errors associated with the retrieval of O_2, such as the airmass dependence of the O_2 column, will affect XCO_2. Figure 8 is XCO_2 calculated for four different combinations pertaining to the two CO_2 column retrievals and

the O_2 column retrievals. The CO_2 columns were retrieved with either a Voigt line shape (the standard GGG2014 approach) or the qSDV with line mixing as done in Mendonca et al. (2016) while the O_2 columns were retrieved with either a Voigt (the standard GGG2014 approach) or the new qSDV approach developed here. Figure 8 shows a spurious symmetric component to XCO_2 when the total column of O_2 is retrieved with the Voigt line shape, regardless of line shape used to retrieve CO_2. When the qSDV is used to retrieve total columns of O_2, the symmetric component of XCO_2 is dismissed regardless of line shape used to retrieve CO_2. This is because the airmass dependence of the column of O_2 retrieved using the qSDV is more consistent with the airmass dependence of the column of CO_2 (for both line shapes used to retrieve CO_2). Mendonca et al. (2016) showed that using the qSDV with line mixing results in better fits to the CO_2 windows and impacts the airmass dependence of the retrieved column of CO_2. When using a Voigt line shape the retrieved column amount of CO_2 decreases as airmass increases until the airmass is large (SZA of about 82º) at which point the retrieved column of CO_2 increases as the airmass increases, changing the shape of the airmass dependence of the CO_2 column. When the qSDV with line mixing is used, the retrieved column of CO_2 decreases as a function of airmass (up until the sun is above the horizon).

~~In order to~~ To correct for this, an empirical correction is applied to all TCCON XCO_2 (and XGas). The empirical correction determines the antisymmetrical component of the day's XCO_2, which is assumed to be the true variation of XCO_2 throughout the day, as well as the symmetrical component, which is caused by the airmass dependence of the retrieved column of the gas of interest and O_2. We can, therefore, represent a measurement as (Wunch et al., 2011):

$$y_i = \hat{y}[1 + \alpha S(\theta_i) + \beta A(t_i)] \quad (5)$$

where $\hat{y}$ is the mean value of XCO_2 measured that day, β is the fitted coefficient of the antisymmetric function $A(t_i)$ and α is the fitted coefficient of the symmetric function $S(\theta_i)$. The antisymmetric function is calculated by (Wunch et al., 2011):

$$A(t_i) = \sin(2\pi(t_i - t_{noon})) \quad (6)$$

where t_i is the time of the measurement and t_{noon} is the time at solar noon, both in units of days. The symmetric function is calculated by (Wunch et al., 2011):

$$S(\theta_i) = \left(\frac{\theta_i + 13^o}{90^o + 13^o}\right)^3 - \left(\frac{~~\theta_i~~45^o + 13^o}{90^o + 13^o}\right)^3 \quad (7)$$

where θ_i is the SZA in degrees. To determine α for the different line shapes, total columns of CO_2 were retrieved using the Voigt line shape (Wunch, D. et al., 2015) and the qSDV with line mixing (Mendonca et al., 2016). Henceforth, we will refer to XCO_2 calculated from O_2 and CO_2 using the Voigt line shape as XCO_2 Voigt and the qSDV line shape as XCO_2 qSDV.

Figure 9~~7~~ shows the average α calculated for each season at Darwin, Lamont, and Park Falls. Eureka XCO_2 cannot be used to determine α because Eureka measurements do not go through the same range of SZAs as the other three

sites due to its geolocation. The average α values derived from XCO_2 Voigt are represented by stars in Figure 9~~7~~, while the squares indicate XCO_2 qSDV. At all three sites, α is closer to 0 when the qSDV line shape is used in the retrieval compared to the Voigt retrieval, regardless of the season. The average α for XCO_2 Voigt calculated from a year of measurements from Darwin, Park Falls, and Lamont is -0.0071±0.0057 and that for XCO_2 qSDV is -0.0012±0.0054.

For all four sites, α = -0.0071 is used to correct XCO_2 Voigt measurements. Figure 10~~8~~a shows the XCO_2 Voigt anomalies plotted as a function of SZA. The data is expressed as the daily XCO_2 anomaly, which is the difference between the XCO_2 value and the daily median value, in order to remove the seasonal cycle. When XCO_2 is left uncorrected for airmass dependencies, ~~there is a clear airmass dependence where the amount of~~ XCO_2 decreases as a function of SZA up to ~~a SZA of~~ approximately 82º, ~~at which point XCO_2~~ and increases as a function of SZA at andgles greater than 82º. Figure 10~~8~~b shows XCO_2 Voigt corrected for the airmass dependence. This airmass correction works well only up to a SZA of approximately 82º~~, after which the correction only serves to increase the airmass dependence~~. Figure 10~~8~~c is the same as 10~~8~~a but for the uncorrected XCO_2 qSDV measurements, while Figure 10~~8~~d is the same as 10~~8~~b but for the corrected XCO_2 qSDV measurements. When the airmass correction is applied to XCO_2 qSDV there is a small difference between the corrected and uncorrected XCO_2 qSDV measurements, with the difference only noticeable for the Darwin measurements recorded at SZA > 60º. For XCO_2 qSDV measurements made at SZA > 82º XCO_2 does not increase with SZA as it does with the Voigt.

5.2 Accuracy of XCO_2

To assess the accuracy of TCCON XCO_2 measurements, they are compared to aircraft XCO_2 profile measurements using the method described in Wunch et al. (2010). Figure 11~~9~~a shows the comparison between the aircraft XCO_2 measurements (legend ~~on~~ at the top details the different aircraft) and TCCON XCO_2 Voigt measurements for 13 TCCON sites (given by the color-coded legend ~~on~~ at the bottom right). The gray line indicates the one-to-one line and the dashed line is the line of best fit. There is a bias of 0.9897±0.0005, as given by the slope of the line of best fit in Figure 11~~9~~a, for the XCO_2 Voigt measurements. Figure 11~~9~~b is the same as 11~~9~~a but for the XCO_2 qSDV measurements. The bias between the aircraft XCO_2 measurements and the XCO_2 qSDV measurements is 1.0041±0.0005 as given by the slope of the line of best fit in Figure 11~~9~~b. This increase in the slope can be explained by an increase in the retrieved column of CO_2 when using the qSDV with line mixing as shown in Mendonca et al. (2016) as well as combined with a decrease in the retrieved O_2 column due to using the qSDV. As discussed previously (section 5) the decrease in the retrieved O_2 column is an improvement but the expected column of O_2 is still approximately 1.2% higher (at the smallest SZA) than it should be. Therefore, the retrieved column of CO_2 is higher than it should be, and the slope would be greater if the retrieved column of O_2 was 1.2% lower. Never the less ~~Using~~ using the qSDV to retrieve total columns of CO_2 and O_2 ~~thus~~ reduces the difference between TCCON XCO_2 and aircraft XCO_2 measurements by 0.62 %.

TCCON XCO_2 measurements are divided by the scale factors (or bias determined in Figure 11~~9~~) to calibrate to the WMO scale. For all TCCON XCO_2 measurements retrieved with a Voigt line shape, the airmass correction is first

applied to the data and the result is divided by the determined bias factor, 0.9897. Figure 12~~10~~a to 12~~10~~d shows XCO_2 Voigt (for Eureka, Park Falls, Lamont, and Darwin respectively) indicated by red square boxes in the plots. XCO_2 Voigt measurements made at SZA > 82° have been filtered out because they cannot be corrected for the airmass dependence. The blue boxes are XCO_2 qSDV corrected for airmass dependence and scaled by 1.0041. No filter was applied to the XCO_2 qSDV measurements for SZA since the airmass dependence correction works at all SZA. Figure 12~~10~~e to 12~~10~~h shows the difference between XCO_2 Voigt and XCO_2 qSDV for Eureka, Park Falls, Lamont, and Darwin respectively. The mean differences for the data shown in Figures 12~~10~~e to 12~~10~~h are 0.113±0.082, -0.102±0.223, -0.132±0.241, and -0.059±0.231 µmol/mol (ppm) for Eureka, Park Falls, Lamont, and Darwin respectively. The difference throughout the day at Park Falls, Lamont, and Darwin varies between -0.6 to 0.2 µmol/mol and is SZA dependent.

Figure 13~~11~~a shows XCO_2 Voigt corrected for the airmass dependence, as well as XCO_2 qSDV, uncorrected and corrected for the airmass dependence. These XCO_2 measurements were retrieved from Park Falls spectra recorded on June 18, 2013. For all three XCO_2 measurements, the amount of XCO_2 decreases throughout the day. Figure 13~~11~~b shows the difference between the corrected Voigt XCO_2 and the uncorrected qSDV XCO_2, as well as the difference between the corrected Voigt XCO_2 and the corrected qSDV XCO_2. The difference between the Voigt and the qSDV (corrected and uncorrected) shows that at the start and end of the day, more XCO_2 is retrieved with the qSDV, while at midday less is retrieved with the qSDV. The range in the differences seen in Figure 12~~10~~e to 12~~10~~h varies with SZA throughout the day as shown in Figure 13~~11~~b.

6. Discussion and Conclusions

Using cavity ring-down spectra measured in the lab, we have shown that the Voigt line shape is insufficient to model the line shape of O_2 for the 1.27 µm band, consistent with the results of(Hartmann et al. (2013) and Lamouroux et al. (2014). By using the speed-dependent Voigt line shape when calculating the absorption coefficients, we were better able to reproduce the measured absorption coefficients than using the Voigt line shape. However, some residual structure ~~still~~ remains as seen Figures 1 and 2. This is partly due to the blending of spectral lines (i.e., line mixing) and the inability to retrieve the spectroscopic parameters for weak O_2 transitions. Fitting low-pressure spectra would help with isolating spectral lines and decreasing the uncertainty on the retrieved spectroscopic parameters for the Q branch lines.

Accurate measurements of the pressure shifts in the 1.27 µm band have been hard to obtain as shown in Newman et al. (1999) and Hill et al., (2003). While the retrieved pressure shifts show a dependence on quantum number m (Figure 3c) as one would expect, this dependence is not as strong as the m dependence of the Lorentz widths (Figure 3b). This can be explained by the fact that line mixing, which is shown to be important for the O_2 A-band, was not considered when fitting the cavity-ringdown spectra. Neglecting line mixing usually produces an asymmetric residual in the discrete lines as well as a broad residual feature associated with the fact that collisions are transferring intensity from one part of the spectrum to another. By fitting a set of Legendre polynomials for CIA we could be simultaneously fitting the broader band feature associated with line mixing while the retrieved pressure shifts, and

speed-dependent pressure shifts could be compensating for the asymmetric structure one would see in the discrete lines when neglecting line mixing. The remaining structure, as seen in Figure 1c, could be due to neglecting line mixing especially in the Q-branch where the spacing between spectral lines is small (in comparison to the P and R branches) and line mixing is most likely prevalent.

The pressure dependence of the retrieved speed-dependent width parameter is an indication that Dicke narrowing needs to be taken into account, as shown by Bui et al. (2014) for CO_2. ~~However, when~~ When ~~dealing with~~ both speed dependence and Dicke narrowing are present, a multi-spectrum fit needs to be used due to the correlation between the parameters (Bui et al., 2014). Domysławska et al. (2016) recommend using the qSDV to model the line shape of O_2 based on multiple line shape studies of the O_2 B-band. In these studies, a multi-spectrum fit to low pressure (0.27-5.87 kPa) cavity-ring down spectra was preformed testing multiple line shapes that took speed-dependence and Dicke narrowing into account both separately and simultaneously. They found that the line shapes that only used Dicke narrowing were not good enough to model the line shape of the O_2 B-band lines, but a line shape that included either speed-dependence or both speed-dependence and Dicke narrowing produced similar quality fits, ultimately concluding that speed-dependence has a larger effect than Dicke narrowing. It was noted in the study by Wójtewicz et al., (2014) that both Dicke narrowing and speed-dependent effects might simultaneously play an important role in modeling the line shape of the O_2 B-band lines. However, the speed-dependent and Dicke narrowing parameters are highly correlated at low pressures. To reduce the correlation requires either a multi-spectrum fit of spectra at low pressures with high enough signal to nosie ratio or spectra that cover a wide range of pressure (Wójtewicz et al., 2014). So, by combining the high-pressure spectra used in this study with low pressure spectra in a multipspectrum fit both the speed-dependence and Dicke narrowing parameters could be retrieved. The temperature dependence of the Lorentz width coefficients of this band has never been measured before, which could have an impact on the airmass dependence of O_2. Combining high-pressure cavity-ring-down absorption coefficient measurements with those for low pressures and different temperatures as done in Devi et al. (2015 and 2016) for CH_4 ~~in~~ would lead to more accurate line shape parameters for O_2.

By taking speed dependence into account for both CO_2 (in the work of Mendonca et al., 2016) and O_2 (the work presented here), we were able to significantly decrease the airmass dependence of TCCON XCO_2 and the bias between TCCON and aircraft XCO_2. With the qSDV line shape, XCO_2 measurements made at SZA > 82° no longer have to be discarded, resulting in more XCO_2 measurement available from all TCCON sites. This is particularly important for high-latitude TCCON sites, such as Eureka, because measurements made from late February to late March and from late September until mid-October are made at SZA > 82°. Filtering out these large SZA measurements thus limits the knowledge of the seasonal cycle of XCO_2 at high latitudes. The airmass dependence of the O_2 column not only effects XCO_2 but all trace gases measured by TCCON and in the future the airmass dependence of all XGas will be determined with these new O_2 columns.

Acknowledgements

This work was primarily supported by the Canadian Space Agency (CSA) through the GOSAT and CAFTON projects and the Natural Sciences and Engineering Research Council of Canada (NSERC). The Eureka measurements were made at the Polar Environment Atmospheric Research Laboratory (PEARL) by the Canadian Network for the Detection of Atmospheric Change (CANDAC), which has been supported by the AIF/NSRIT, CFI, CFCAS, CSA, Environment Canada (EC), Government of Canada IPY funding, NSERC, OIT, ORF, PCSP, and FQRNT. The authors wish to thank the staff at EC's Eureka Weather Station and CANDAC for the logistical and on-site support provided. Thanks to CANDAC Principal Investigator James R. Drummond, PEARL Site Manager Pierre Fogal, and CANDAC/PEARL operators Mike Maurice and Peter McGovern, for their invaluable assistance in maintaining and operating the Bruker 125HR. The research at the Jet Propulsion Laboratory (JPL), and California Institute of Technology was performed under contracts and cooperative agreements with the National Aeronautics and Space Administration (NASA). Geoff Toon and Debra Wunch acknowledge support from NASA for the development of TCCON via grant number NNX17AE15G. Darwin TCCON measurements are possible thanks to support from NASA grants NAG5-12247 and NNG05-GD07G, the Australian Research Council grants DP140101552, DP110103118, DP0879468 and LP0562346, and the DOE ARM program for technical support. The research at the National Institute of Standards and Technology was performed with the support of the NIST Greenhouse Gas Measurements and Climate Research Program. Certain commercial equipment, instruments, or materials are identified in this paper in order to specify the experimental procedure adequately. Such identification is not intended to imply recommendation or endorsement by the National Institute of Standards and Technology, nor is it intended to imply that the materials or equipment identified are necessarily the best available for the purpose.

References

Abrarov, S.M., Quine, B.M., 2011. Efficient algorithmic implementation of the Voigt/complex error function based on exponential series approximation. Appl. Math. Comput. 218, 1894–1902. https://doi.org/10.1016/j.amc.2011.06.072

Batchelor, R.L., Strong, K., Lindenmaier, R., Mittermeier, R.L., Fast, H., Drummond, J.R., Fogal, P.F., 2009. A New Bruker IFS 125HR FTIR Spectrometer for the Polar Environment Atmospheric Research Laboratory at Eureka, Nunavut, Canada: Measurements and Comparison with the Existing Bomem DA8 Spectrometer. J. Atmospheric Ocean. Technol. 26, 1328–1340. https://doi.org/10.1175/2009JTECHA1215.1

Bergland, G., 1969. A radix-eight fast Fourier transform subroutine for real-valued series. IEEE Trans. Audio Electroacoustics 17, 138–144. https://doi.org/10.1109/TAU.1969.1162043

Bernath, P.F., McElroy, C.T., Abrams, M.C., Boone, C.D., Butler, M., Camy-Peyret, C., Carleer, M., Clerbaux, C., Coheur, P.-F., Colin, R., DeCola, P., DeMazière, M., Drummond, J.R., Dufour, D., Evans, W.F.J., Fast, H., Fussen, D., Gilbert, K., Jennings, D.E., Llewellyn, E.J., Lowe, R.P., Mahieu, E., McConnell, J.C., McHugh, M., McLeod, S.D., Michaud, R., Midwinter, C., Nassar, R., Nichitiu, F., Nowlan, C., Rinsland, C.P., Rochon, Y.J., Rowlands, N., Semeniuk, K., Simon, P., Skelton, R., Sloan, J.J., Soucy, M.-A., Strong, K., Tremblay, P., Turnbull, D., Walker, K.A., Walkty, I., Wardle, D.A., Wehrle, V., Zander, R., Zou, J., 2005. Atmospheric Chemistry Experiment (ACE): Mission overview. Geophys. Res. Lett. 32, L15S01. https://doi.org/10.1029/2005GL022386

Bui, T.Q., Long, D.A., Cygan, A., Sironneau, V.T., Hogan, D.W., Rupasinghe, P.M., Ciuryło, R., Lisak, D., Okumura, M., 2014. Observations of Dicke narrowing and speed dependence in air-broadened CO_2 lineshapes near 2.06 μm. J. Chem. Phys. 141, 174301. https://doi.org/10.1063/1.4900502

Cheah, S.-L., Lee, Y.-P., Ogilvie, J.F., 2000. Wavenumbers, strengths, widths and shifts with pressure of lines in four bands of gaseous $^{16}O_2$ in the systems $a^1\Delta_g^- X^3\Sigma_g^-$ and $b^1\Sigma_g^+ - X^3\Sigma_g^-$. J. Quant. Spectrosc. Radiat. Transf. 64, 467–482. https://doi.org/10.1016/S0022-4073(99)00126-0

Ciuryło, R., 1998. Shapes of pressure- and Doppler-broadened spectral lines in the core and near wings. Phys. Rev. A 58, 1029–1039. https://doi.org/10.1103/PhysRevA.58.1029

Crisp, D., Atlas, R.M., Breon, F.-M., Brown, L.R., Burrows, J.P., Ciais, P., Connor, B.J., Doney, S.C., Fung, I.Y., Jacob, D.J., Miller, C.E., O'Brien, D., Pawson, S., Randerson, J.T., Rayner, P., Salawitch, R.J., Sander, S.P., Sen, B., Stephens, G.L., Tans, P.P., Toon, G.C., Wennberg, P.O., Wofsy, S.C., Yung, Y.L., Kuang, Z., Chudasama, B., Sprague, G., Weiss, B., Pollock, R., Kenyon, D., Schroll, S., 2004. The Orbiting Carbon Observatory (OCO) mission. Adv. Space Res., Trace Constituents in the Troposphere and Lower Stratosphere 34, 700–709. https://doi.org/10.1016/j.asr.2003.08.062

Deutscher, N.M., Griffith, D.W.T., Bryant, G.W., Wennberg, P.O., Toon, G.C., Washenfelder, R.A., Keppel-Aleks, G., Wunch, D., Yavin, Y., Allen, N.T., Blavier, J.-F., Jiménez, R., Daube, B.C., Bright, A.V., Matross, D.M., Wofsy, S.C., Park, S., 2010. Total column CO_2 measurements at Darwin, Australia – site description and calibration against in situ aircraft profiles. Atmos Meas Tech 3, 947–958. https://doi.org/10.5194/amt-3-947-2010

Devi, V.M., Benner, D.C., Sung, K., Brown, L.R., Crawford, T.J., Yu, S., Smith, M.A.H., Mantz, A.W., Boudon, V., Ismail, S., 2016. Spectral line parameters including line shapes in the $2\nu_3$ Q branch of $^{12}CH_4$. J. Quant. Spectrosc. Radiat. Transf., XVIIIth Symposium on High Resolution Molecular Spectroscopy (HighRus-2015), Tomsk, Russia 177, 152–169. https://doi.org/10.1016/j.jqsrt.2015.12.009

Devi, V.M., Benner, D.C., Sung, K., Crawford, T.J., Yu, S., Brown, L.R., Smith, M.A.H., Mantz, A.W., Boudon, V., Ismail, S., 2015. Self- and air-broadened line shapes in the $2\nu_3$ P and R branches of 12CH4. J. Mol. Spectrosc., Spectroscopy with Synchrotron Radiation 315, 114–136. https://doi.org/10.1016/j.jms.2015.05.003

Dicke, R.H., 1953. The Effect of Collisions upon the Doppler Width of Spectral Lines. Phys. Rev. 89, 472–473. https://doi.org/10.1103/PhysRev.89.472

Domysławska, J., Wójtewicz, S., Masłowski, P., Cygan, A., Bielska, K., Trawiński, R.S., Ciuryło, R., Lisak, D., 2016. A new approach to spectral line shapes of the weak oxygen transitions for atmospheric applications. J. Quant. Spectrosc. Radiat. Transf. 169, 111–121. https://doi.org/10.1016/j.jqsrt.2015.10.019

Drouin, B.J., Benner, D.C., Brown, L.R., Cich, M.J., Crawford, T.J., Devi, V.M., Guillaume, A., Hodges, J.T., Mlawer, E.J., Robichaud, D.J., Oyafuso, F., Payne, V.H., Sung, K., Wishnow, E.H., Yu, S., 2017.

Multispectrum analysis of the oxygen A-band. J. Quant. Spectrosc. Radiat. Transf., Satellite Remote Sensing and Spectroscopy: Joint ACE-Odin Meeting, October 2015 186, 118–138. https://doi.org/10.1016/j.jqsrt.2016.03.037

Gordon, I.E., Kassi, S., Campargue, A., Toon, G.C., 2010. First identification of the electric quadrupole transitions of oxygen in solar and laboratory spectra. J. Quant. Spectrosc. Radiat. Transf., Special Issue Dedicated to Laurence S. Rothman on the Occasion of his 70th Birthday. 111, 1174–1183. https://doi.org/10.1016/j.jqsrt.2010.01.008

Gordon, I.E., Rothman, L.S., Hill, C., Kochanov, R.V., Tan, Y., Bernath, P.F., Birk, M., Boudon, V., Campargue, A., Chance, K.V., Drouin, B.J., Flaud, J.-M., Gamache, R.R., Hodges, J.T., Jacquemart, D., Perevalov, V.I., Perrin, A., Shine, K.P., Smith, M.-A.H., Tennyson, J., Toon, G.C., Tran, H., Tyuterev, V.G., Barbe, A., Császár, A.G., Devi, V.M., Furtenbacher, T., Harrison, J.J., Hartmann, J.-M., Jolly, A., Johnson, T.J., Karman, T., Kleiner, I., Kyuberis, A.A., Loos, J., Lyulin, O.M., Massie, S.T., Mikhailenko, S.N., Moazzen-Ahmadi, N., Müller, H.S.P., Naumenko, O.V., Nikitin, A.V., Polyansky, O.L., Rey, M., Rotger, M., Sharpe, S.W., Sung, K., Starikova, E., Tashkun, S.A., Auwera, J.V., Wagner, G., Wilzewski, J., Wcisło, P., Yu, S., Zak, E.J., 2017. The HITRAN2016 molecular spectroscopic database. J. Quant. Spectrosc. Radiat. Transf., HITRAN2016 Special Issue 203, 3–69. https://doi.org/10.1016/j.jqsrt.2017.06.038

Griffith, D.W.T., Deutscher, N.M., Velazco, V.A., Wennberg, P.O., Yavin, Y., Keppel-Aleks, G., Washenfelder, R.A., Toon, G.C., Blavier, J.-F., Paton-Walsh, C., Jones, N.B., Kettlewell, G.C., Connor, B.J., Macatangay, R.C., Roehl, C., Ryczek, M., Glowacki, J., Culgan, T., Bryant, G.W., 2017. TCCON data from Darwin (AU), Release GGG2014.R0. https://doi.org/10.14291/tccon.ggg2014.darwin01.R0/1149290

Hartmann, J.-M., Sironneau, V., Boulet, C., Svensson, T., Hodges, J.T., Xu, C.T., 2013. Collisional broadening and spectral shapes of absorption lines of free and nanopore-confined O_2 gas. Phys. Rev. A 87, 032510. https://doi.org/10.1103/PhysRevA.87.032510

Hill, C., Brown, J.M., Newnham, D.A., 2003. An upper limit for the magnitude of pressure shifts in the O_2 $a^1\Delta g \leftarrow X^3\Sigma^-_g(0–0)$ band. J. Mol. Spectrosc. 221, 286–287. https://doi.org/10.1016/S0022-2852(03)00227-3

Hodges, J.T., 2005. Automated high-resolution frequency-stabilized cavity ring-down absorption spectrometer. Rev. Sci. Instrum. 76, 023112. https://doi.org/10.1063/1.1850633

Hodges, J.T., Layer, H.P., Miller, W.., Scace, G.E., 2004. Frequency-stabilized single-mode cavity ring-down apparatus for high-resolution absorption spectroscopy. Rev. Sci. Instrum. 75, 849–863. https://doi.org/10.1063/1.1666984

Keppel-Aleks, G., Toon, G.C., Wennberg, P.O., Deutscher, N.M., 2007. Reducing the impact of source brightness fluctuations on spectra obtained by Fourier-transform spectrometry. Appl. Opt. 46, 4774. https://doi.org/10.1364/AO.46.004774

Lamouroux, J., Sironneau, V., Hodges, J.T., Hartmann, J.-M., 2014. Isolated line shapes of molecular oxygen: Requantized classical molecular dynamics calculations versus measurements. Phys. Rev. A 89, 042504. https://doi.org/10.1103/PhysRevA.89.042504

Leshchishina, O., Kassi, S., Gordon, I.E., Rothman, L.S., Wang, L., Campargue, A., 2010. High sensitivity CRDS of the $a^1\Delta_g^- X^3\Sigma_g^-$ band of oxygen near 1.27 μm: Extended observations, quadrupole transitions, hot bands and minor isotopologues. J. Quant. Spectrosc. Radiat. Transf., XVIth Symposium on High Resolution Molecular Spectroscopy (HighRus-2009) XVIth Symposium on High Resolution Molecular Spectroscopy 111, 2236–2245. https://doi.org/10.1016/j.jqsrt.2010.05.014

Leshchishina, O., Kassi, S., Gordon, I.E., Yu, S., Campargue, A., 2011. The band of $^{16}O^{17}O$, $^{17}O^{18}O$ and $^{17}O_2$ by high sensitivity CRDS near 1.27 μm. J. Quant. Spectrosc. Radiat. Transf. 112, 1257–1265. https://doi.org/10.1016/j.jqsrt.2011.01.014

Lévy, A., Lacome, N., Chackerian Jr., C., 1992. Collisional Line Mixing A2 - Weber, K. Narahari RaoAlfons, in: Spectroscopy of the Earth's Atmosphere and Interstellar Medium. Academic Press, pp. 261–337.

Lin, H., Reed, Z.D., Sironneau, V.T., Hodges, J.T., 2015. Cavity ring-down spectrometer for high-fidelity molecular absorption measurements. J. Quant. Spectrosc. Radiat. Transf. 161, 11–20. https://doi.org/10.1016/j.jqsrt.2015.03.026

Long, D.A., Havey, D.K., Okumura, M., Miller, C.E., Hodges, J.T., 2010. O_2 A-band line parameters to support atmospheric remote sensing. J. Quant. Spectrosc. Radiat. Transf. 111, 2021–2036. https://doi.org/10.1016/j.jqsrt.2010.05.011

Maté, B., Lugez, C., Fraser, G.T., Lafferty, W.J., 1999. Absolute intensities for the O_2 1.27 μm continuum absorption. J. Geophys. Res. Atmospheres 104, 30585–30590. https://doi.org/10.1029/1999JD900824

Mendonca, J., Strong, K., Toon, G.C., Wunch, D., Sung, K., Deutscher, N.M., Griffith, D.W.T., Franklin, J.E., 2016. Improving atmospheric CO_2 retrievals using line mixing and speed-dependence when fitting high-

resolution ground-based solar spectra. J. Mol. Spectrosc., Atmospheric Spectroscopy 323, 15–27. https://doi.org/10.1016/j.jms.2016.01.007

Mertz, L., 1967. Auxiliary computation for Fourier spectrometry. Infrared Phys. 7, 17–23. https://doi.org/10.1016/0020-0891(67)90026-7

Mlawer, E.J., Clough, S.A., Brown, P.D., Stephen, T.M., Landry, J.C., Goldman, A., Murcray, F.J., 1998. Observed atmospheric collision-induced absorption in near-infrared oxygen bands. J. Geophys. Res. Atmospheres 103, 3859–3863. https://doi.org/10.1029/97JD03141

Newman, S.M., Lane, I.C., Orr-Ewing, A.J., Newnham, D.A., Ballard, J., 1999. Integrated absorption intensity and Einstein coefficients for the O_2 $a^1\Delta_g$–$X^3\Sigma_g^-$ (0,0) transition: A comparison of cavity ringdown and high resolution Fourier transform spectroscopy with a long-path absorption cell. J. Chem. Phys. 110, 10749–10757. https://doi.org/10.1063/1.479018

Newman, S.M., Orr-Ewing, A.J., Newnham, D.A., Ballard, J., 2000. Temperature and pressure dependence of line widths and integrated absorption intensities for the O_2 $a^1\Delta_g$ - $X^3\sum_g^-$ (0,0) transition. J. Phys. Chem. A 104, 9467–9480.

Ngo, N.H., Lisak, D., Tran, H., Hartmann, J.-M., 2013. An isolated line-shape model to go beyond the Voigt profile in spectroscopic databases and radiative transfer codes. J. Quant. Spectrosc. Radiat. Transf. 129, 89–100. https://doi.org/10.1016/j.jqsrt.2013.05.034

Predoi-Cross, A., Hambrook, K., Keller, R., Povey, C., Schofield, I., Hurtmans, D., Over, H., Mellau, G.C., 2008. Spectroscopic lineshape study of the self-perturbed oxygen A-band. J. Mol. Spectrosc. 248, 85–110. https://doi.org/10.1016/j.jms.2007.11.007

Rohart, F., Mäder, H., Nicolaisen, H.-W., 1994. Speed dependence of rotational relaxation induced by foreign gas collisions: Studies on CH_3F by millimeter wave coherent transients. J. Chem. Phys. 101, 6475–6486. https://doi.org/10.1063/1.468342

Rothman, L.S., Gordon, I.E., Babikov, Y., Barbe, A., Chris Benner, D., Bernath, P.F., Birk, M., Bizzocchi, L., Boudon, V., Brown, L.R., Campargue, A., Chance, K., Cohen, E.A., Coudert, L.H., Devi, V.M., Drouin, B.J., Fayt, A., Flaud, J.-M., Gamache, R.R., Harrison, J.J., Hartmann, J.-M., Hill, C., Hodges, J.T., Jacquemart, D., Jolly, A., Lamouroux, J., Le Roy, R.J., Li, G., Long, D.A., Lyulin, O.M., Mackie, C.J., Massie, S.T., Mikhailenko, S., Müller, H.S.P., Naumenko, O.V., Nikitin, A.V., Orphal, J., Perevalov, V., Perrin, A., Polovtseva, E.R., Richard, C., Smith, M.A.H., Starikova, E., Sung, K., Tashkun, S., Tennyson, J., Toon, G.C., Tyuterev, V.G., Wagner, G., 2013b. The HITRAN2012 molecular spectroscopic database. J. Quant. Spectrosc. Radiat. Transf., HITRAN2012 special issue 130, 4–50. https://doi.org/10.1016/j.jqsrt.2013.07.002

Rothman, L.S., Gordon, I.E., Barbe, A., Benner, D.C., Bernath, P.F., Birk, M., Boudon, V., Brown, L.R., Campargue, A., Champion, J.-P., Chance, K., Coudert, L.H., Dana, V., Devi, V.M., Fally, S., Flaud, J.-M., Gamache, R.R., Goldman, A., Jacquemart, D., Kleiner, I., Lacome, N., Lafferty, W.J., Mandin, J.-Y., Massie, S.T., Mikhailenko, S.N., Miller, C.E., Moazzen-Ahmadi, N., Naumenko, O.V., Nikitin, A.V., Orphal, J., Perevalov, V.I., Perrin, A., Predoi-Cross, A., Rinsland, C.P., Rotger, M., Šimečková, M., Smith, M.A.H., Sung, K., Tashkun, S.A., Tennyson, J., Toth, R.A., Vandaele, A.C., Vander Auwera, J., 2009. The HITRAN 2008 molecular spectroscopic database. J. Quant. Spectrosc. Radiat. Transf., HITRAN 110, 533–572. https://doi.org/10.1016/j.jqsrt.2009.02.013

Rothman, L.S., Jacquemart, D., Barbe, A., Chris Benner, D., Birk, M., Brown, L.R., Carleer, M.R., Chackerian Jr., C., Chance, K., Coudert, L.H., Dana, V., Devi, V.M., Flaud, J.-M., Gamache, R.R., Goldman, A., Hartmann, J.-M., Jucks, K.W., Maki, A.G., Mandin, J.-Y., Massie, S.T., Orphal, J., Perrin, A., Rinsland, C.P., Smith, M.A.H., Tennyson, J., Tolchenov, R.N., Toth, R.A., Vander Auwera, J., Varanasi, P., Wagner, G., 2005. The HITRAN 2004 molecular spectroscopic database. J. Quant. Spectrosc. Radiat. Transf. 96, 139–204. https://doi.org/10.1016/j.jqsrt.2004.10.008

Shannon, I., Harris, M., McHugh, D.R., Lewis, E.L., 1986. Low-pressure spectral line profiles: an analysis in terms of symmetric speed-dependent Voigt profiles. J. Phys. B At. Mol. Phys. 19, 1409. https://doi.org/10.1088/0022-3700/19/10/011

Smith, K.M., Newnham, D.A., 2000. Near-infrared absorption cross sections and integrated absorption intensities of molecular oxygen (O_2, O_2-O_2, and O_2-N_2). J. Geophys. Res. Atmospheres 105, 7383–7396. https://doi.org/10.1029/1999JD901171

Smith, K.M., Newnham, D.A., Williams, R.G., 2001. Collision-induced absorption of solar radiation in the atmosphere by molecular oxygen at 1.27 μm: Field observations and model calculations. J. Geophys. Res. Atmospheres 106, 7541–7552. https://doi.org/10.1029/2000JD900699

Strong, K., Mendonca, J., Weaver, D., Fogal, P., Drummond, J.R., Batchelor, R., Lindenmaier, R., 2017. TCCON data from Eureka (CA), Release GGG2014.R1. https://doi.org/10.14291/tccon.ggg2014.eureka01.R1/1325515

Toon, G. C., 2014a. Telluric line list for GGG2014, TCCON data archive. Carbon Dioxide Inf. Anal. Cent. Oak Ridge Natl. Lab. Oak Ridge Tenn. USA. https://doi.org/10.14291/tccon.ggg2014.atm.R0/1221656

Toon, G. C., 2014b. Solar line list for GGG2014. TCCON Data Arch. Hosted Carbon Dioxide Inf. Anal. Cent. Oak Ridge Natl. Lab. Oak Ridge Tenn. USA.

Toon, G.C., 1991. The JPL MkIV interferometer. Opt. Photonics News 2, 19–21. https://doi.org/10.1364/OPN.2.10.000019

Tran, H., Boulet, C., Hartmann, J.-M., 2006. Line mixing and collision-induced absorption by oxygen in the A band: Laboratory measurements, model, and tools for atmospheric spectra computations. J. Geophys. Res. Atmospheres 111, D15210. https://doi.org/10.1029/2005JD006869

Tran, H., Hartmann, J.-M., 2008. An improved O_2 A band absorption model and its consequences for retrievals of photon paths and surface pressures. J. Geophys. Res. Atmospheres 113, D18104. https://doi.org/10.1029/2008JD010011

Tran, H., Ngo, N.H., Hartmann, J.-M., 2013. Efficient computation of some speed-dependent isolated line profiles. J. Quant. Spectrosc. Radiat. Transf. 129, 199–203. https://doi.org/10.1016/j.jqsrt.2013.06.015

Wallace, L., Livingston, W., 1990. Spectroscopic observations of atmospheric trace gases over Kitt Peak. I - Carbon dioxide and methane from 1979 to 1985. J. Geophys. Res. 95, 9823–9827. https://doi.org/10.1029/JD095iD07p09823

Washenfelder, R.A., Toon, G.C., Blavier, J.-F., Yang, Z., Allen, N.T., Wennberg, P.O., Vay, S.A., Matross, D.M., Daube, B.C., 2006. Carbon dioxide column abundances at the Wisconsin Tall Tower site. J. Geophys. Res. Atmospheres 111, D22305. https://doi.org/10.1029/2006JD007154

Wehr, R.A., 2005. Dicke -narrowed spectral lines in carbon monoxide buffered by argon (Ph.D.). University of Toronto (Canada), Canada.

Wennberg, P.O., Roehl, C.M., Wunch, D., Toon, G.C., Blavier, J.-F., Washenfelder, R., Keppel-Aleks, G., Allen, N.T., Ayers, J., 2017a. TCCON data from Park Falls (US), Release GGG2014.R0. https://doi.org/10.14291/tccon.ggg2014.parkfalls01.R0/1149161

Wennberg, P.O., Wunch, D., Roehl, C.M., Blavier, J.-F., Toon, G.C., Allen, N.T., Dowell, P., Teske, K., Martin, C., Martin, J., 2017b. TCCON data from Lamont (US), Release GGG2014.R0. https://doi.org/10.14291/tccon.ggg2014.lamont01.R0/1149159

Wójtewicz, S., Cygan, A., Masłowski, P., Domysławska, J., Lisak, D., Trawiński, R.S., Ciuryło, R., 2014. Spectral line shapes of self-broadened P-branch transitions of oxygen B band. J. Quant. Spectrosc. Radiat. Transf. 144, 36–48. https://doi.org/10.1016/j.jqsrt.2014.03.029

Wunch, D., Toon, G.C., Blavier, J.-F.L., Washenfelder, R.A., Notholt, J., Connor, B.J., Griffith, D.W.T., Sherlock, V., Wennberg, P.O., 2011. The Total Carbon Column Observing Network. Philos. Trans. R. Soc. Math. Phys. Eng. Sci. 369, 2087–2112. https://doi.org/10.1098/rsta.2010.0240

Wunch, D., Toon, G.C., Sherlock, V., Deutscher, N.M., Liu, C., Feist, D.G., Wennberg, P.O., 2015. The Total Carbon Column Observing Network's GGG2014 Data Version. https://doi.org/10.14291/tccon.ggg2014.documentation.R0/ 1221662

Wunch, D., Toon, G.C., Wennberg, P.O., Wofsy, S.C., Stephens, B.B., Fischer, M.L., Uchino, O., Abshire, J.B., Bernath, P., Biraud, S.C., Blavier, J.-F.L., Boone, C., Bowman, K.P., Browell, E.V., Campos, T., Connor, B.J., Daube, B.C., Deutscher, N.M., Diao, M., Elkins, J.W., Gerbig, C., Gottlieb, E., Griffith, D.W.T., Hurst, D.F., Jiménez, R., Keppel-Aleks, G., Kort, E.A., Macatangay, R., Machida, T., Matsueda, H., Moore, F., Morino, I., Park, S., Robinson, J., Roehl, C.M., Sawa, Y., Sherlock, V., Sweeney, C., Tanaka, T., Zondlo, M.A., 2010. Calibration of the Total Carbon Column Observing Network using aircraft profile data. Atmos Meas Tech 3, 1351–1362. https://doi.org/10.5194/amt-3-1351-2010

Yang, Z., Toon, G.C., Margolis, J.S., Wennberg, P.O., 2002. Atmospheric CO_2 retrieved from ground-based near IR solar spectra. Geophys. Res. Lett. 29, 1339. https://doi.org/10.1029/2001GL014537

Yokota, T., Yoshida, Y., Eguchi, N., Ota, Y., Tanaka, T., Watanabe, H., Maksyutov, S., 2009. Global Concentrations of CO_2 and CH_4 Retrieved from GOSAT: First Preliminary Results. Sola 5, 160–163. https://doi.org/10.2151/sola.2009-041

Yu, S., Drouin, B.J., Miller, C.E., 2014. High resolution spectral analysis of oxygen. IV. Energy levels, partition sums, band constants, RKR potentials, Franck-Condon factors involving the $X^3\Sigma_g^-$, $a^1\Delta_g$ and $b^1\Sigma_g^+$ states. J. Chem. Phys. 141, 174302. https://doi.org/10.1063/1.4900510

Figures

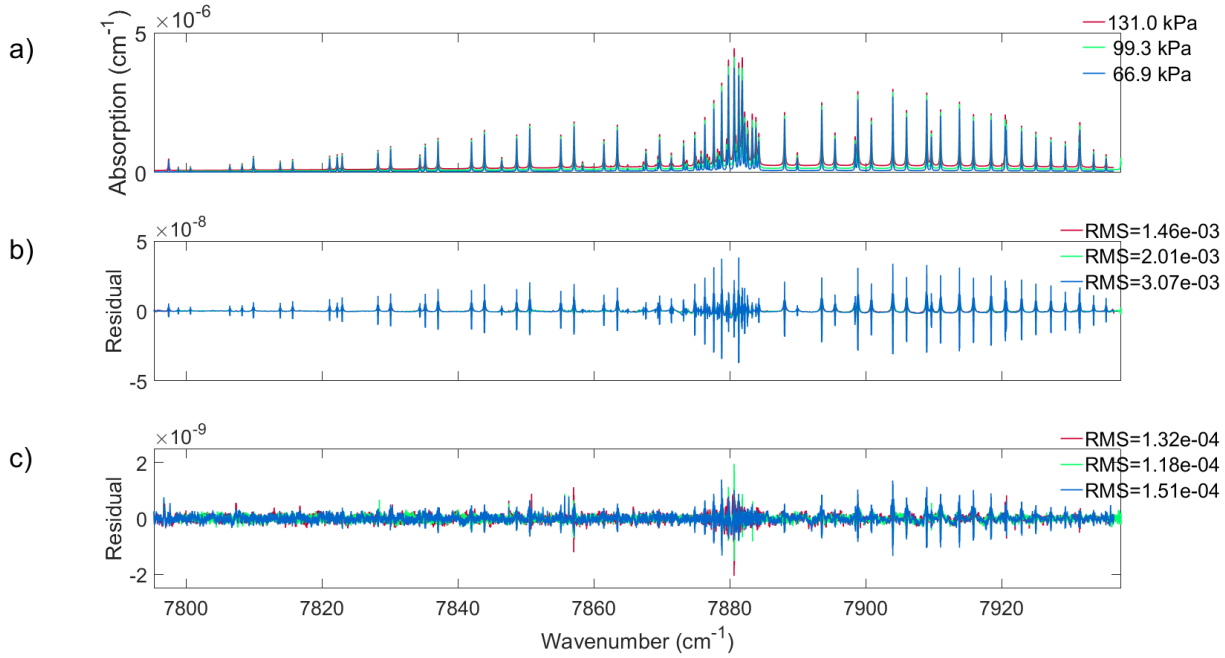

Figure 1: (a) Cavity-ring-down absorption coefficients for O_2 measured at the three pressures indicated in the legend at approximately room temperature and a volume mixing ratio of 0.20720(43) ~~for O_2~~. The difference between measured absorption coeffcients and those calculated using (b) a Voigt line shape, and (c) the speed-dependent Voigt line shape. Note the difference in scale between panels (b) and (c).

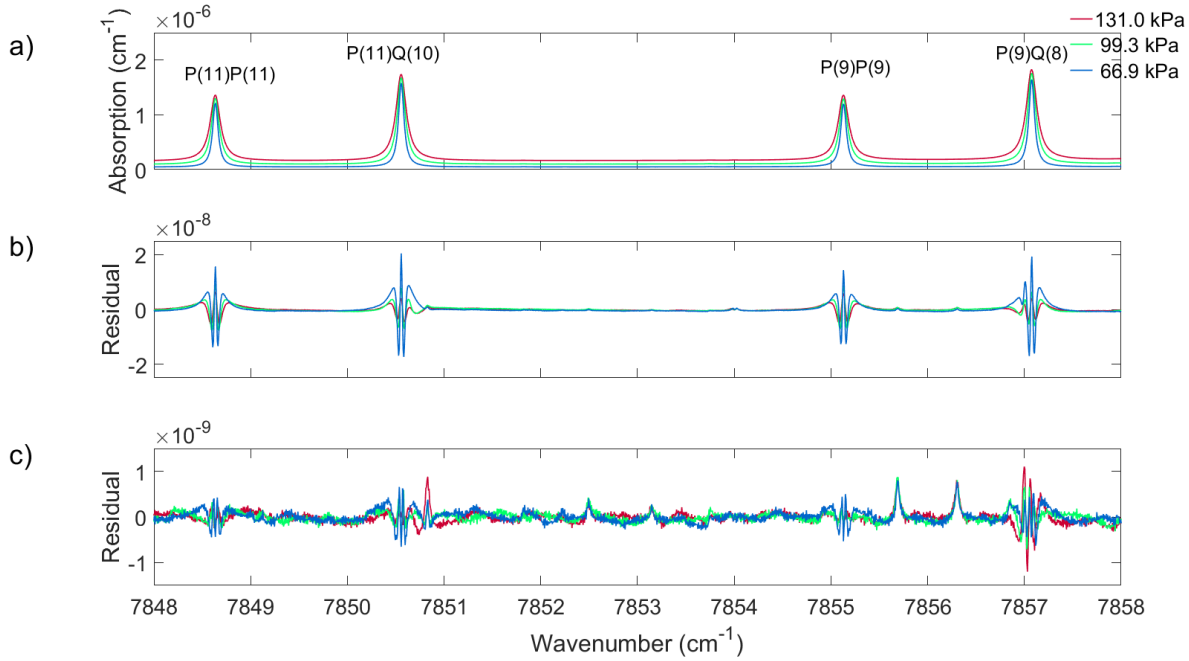

Figure 2: The same as Figure 1 but ~~zoomed into~~ expanded to show four spectral lines in the P branch of the O_2 1.27 µm band.

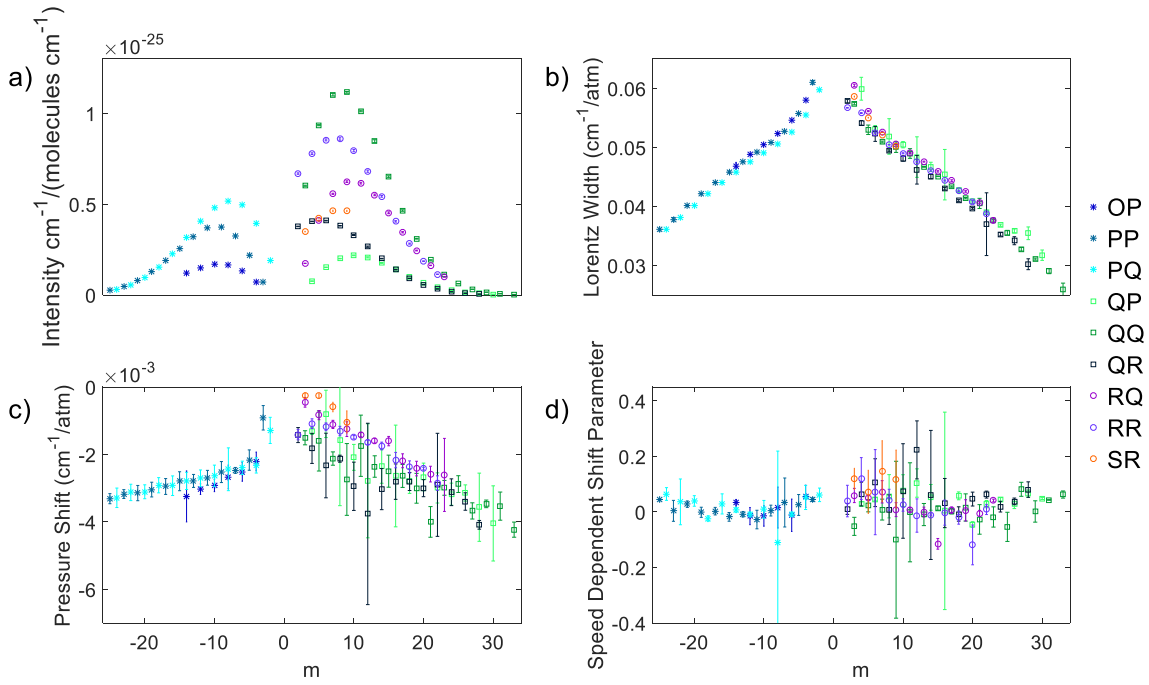

Figure 3: The averaged measured (a) intensity, (b) Lorentz line width, (c) pressure shift, and (d) speed-dependent pressure shift retrieved from the three cavity ring-down spectra of the 1.27 μm band of O_2. All data are plotted as a function of ~~lower state rotational quantum number J~~ m which is m =-J for the P-branch lines, m=J for the Q-branch, and m=J+1 for the R-branch (where J is the lower state rotational quantum number) and the uncertainties shown are 2σ.

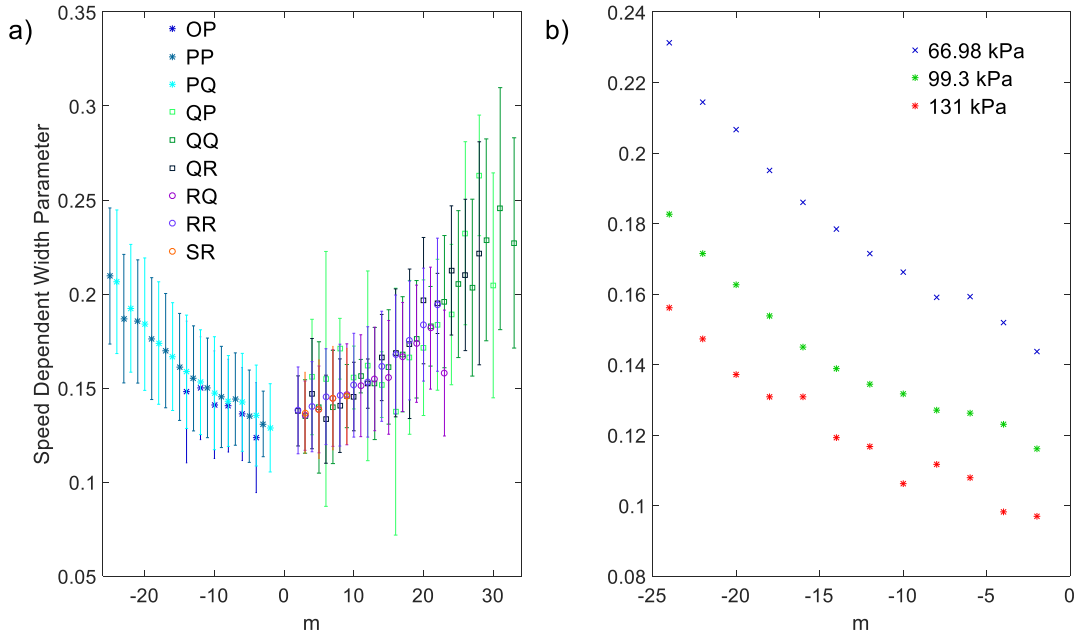

Figure 4: (a) The averaged measured speed-dependent width parameter of the 1.27 μm band of O_2 plotted as a function of m.~~lower state rotational quantum number J''.~~ (b) The measured speed-dependent width parameter for spectral lines that belong to the PQ sub-branch plotted as a function of m.~~lower state rotational quantum number J''.~~

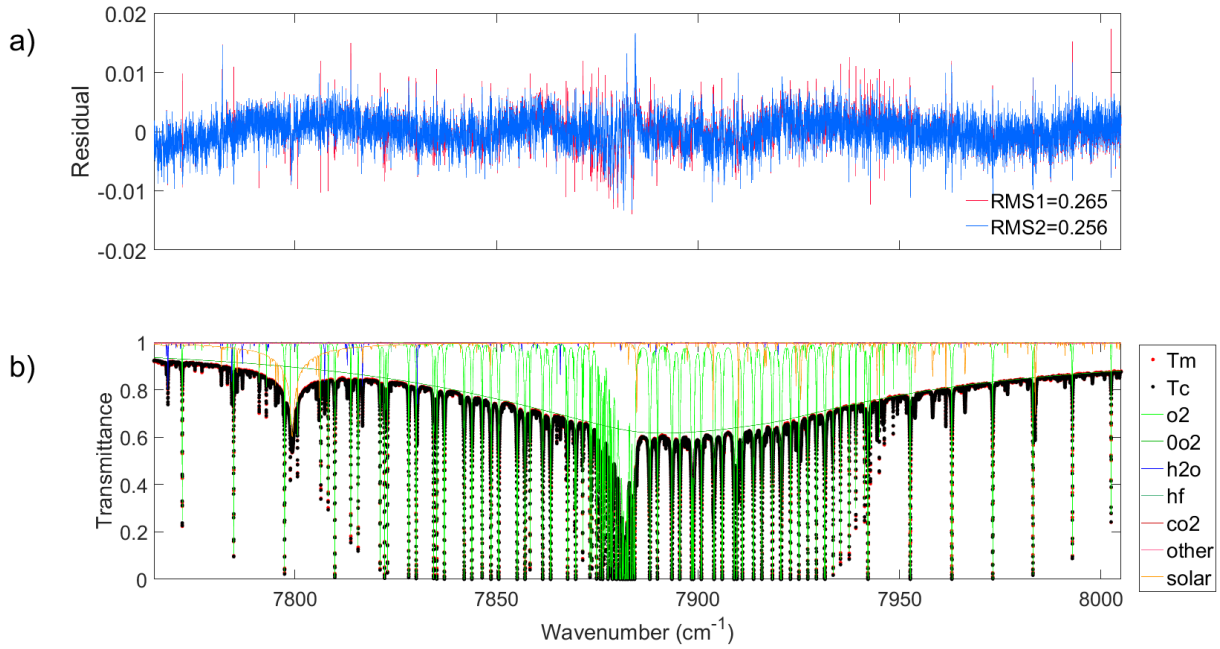

693

694 **Figure 5: (a) The residuals (measured minus calculated) for a spectrum measured at Eureka on March 27,**
695 **2015 at a SZA of 81.32º. The red residual is the result of using the Voigt line shape and the blue is from using**
696 **the qSDV. (b) The measured (red dots) and calculated (black dots), with the qSDV, spectrum, along with the**
697 **gases included in the fit (refer to the legend to the right) in the spectral window.**

698

699

700

701

702

703

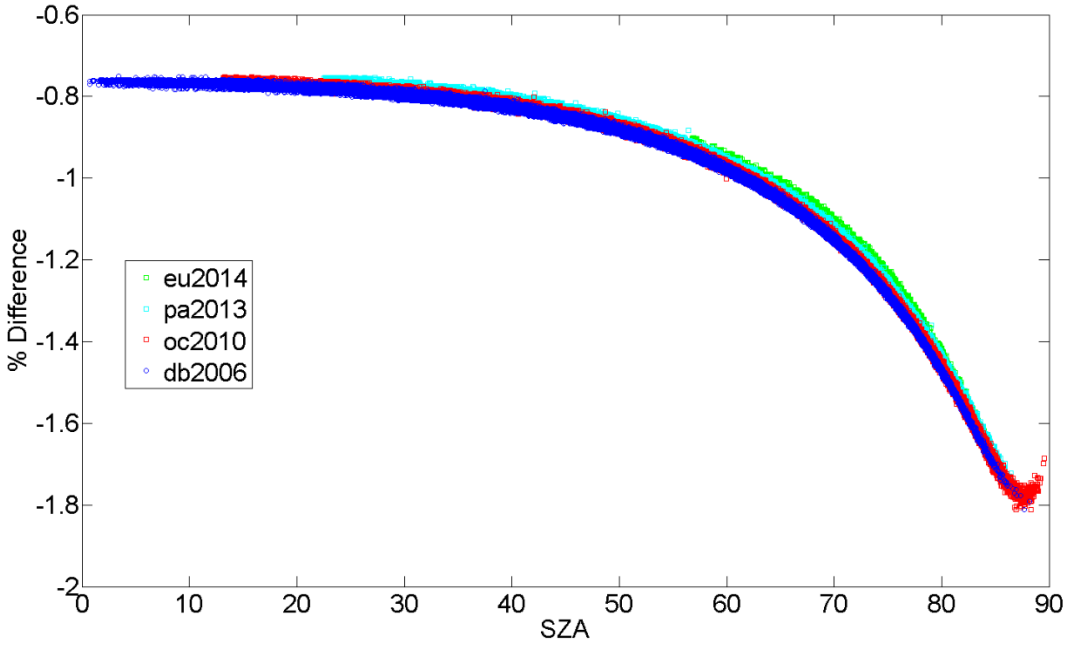

704

705 **Figure 6: The percent difference between the O_2 column retrieved with the Voigt and qSDV line shapes for a**
706 **year of measurements from Eureka (eu), Park Falls (pa), Lamont (oc), and Darwin (db).**

707

708

709

710

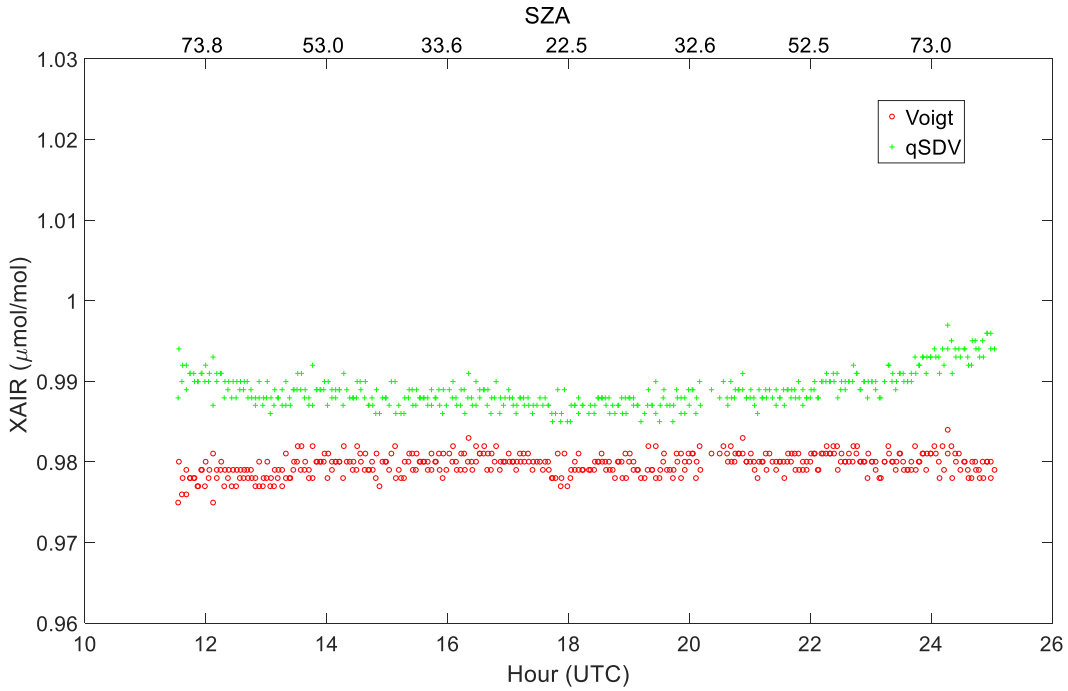

711

712 **Figure 7: XAIR from Park Falls retrieved from spectra recorded on June 18, 2013. XAIR is calculated using**
713 **O_2 columns retrieved using a Voigt (red) and qSDV (green) line shapes. The top x-axis is the SZA that**
714 **corresponds to the hour on the bottom x-axis.**

715

716

717

718

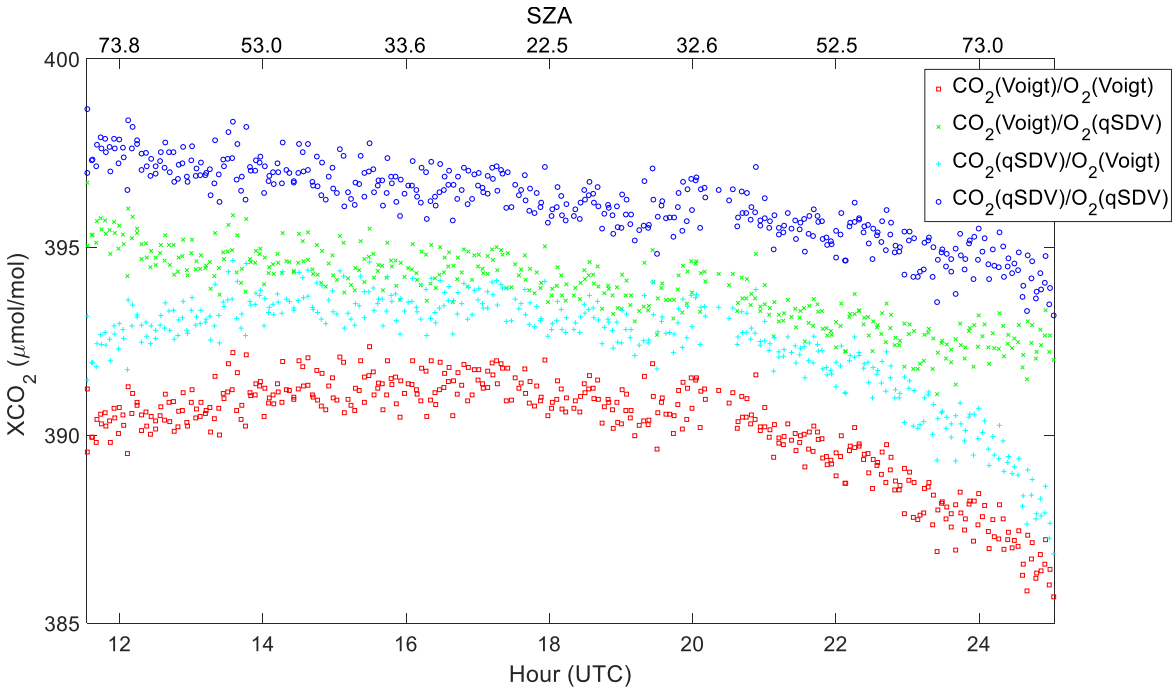

719

720 **Figure 8: XCO_2 calculated from the CO_2 and O_2 columns retrieved from Park Falls spectra recorded on June**
721 **18, 2013. The CO_2 columns were retrievied using either the Voigt line shape or the qSDV with line mixing,**
722 **while the O_2 columns were retrieved using either the Voigt or qSDV line shapes. XCO_2 was calculated in**
723 **four ways: 1) Both CO_2 and O_2 columns retrieved using the Voigt line shape (red), 2) CO_2 columns retrieved**
724 **with the Voigt and O_2 columns retrieved with the qSDV (green), 3) CO_2 columns retrieved with the qSDV**
725 **and line mixing and O_2 columns retrieved with the Voigt (cyan), and 4) CO_2 columns retrieved with the qSDV**
726 **and line mixing and O_2 columns retrieved with the qSDV (blue). The top x-axis is the SZA that corresponds**
727 **to the hour on the bottom x-axis.**

728

729

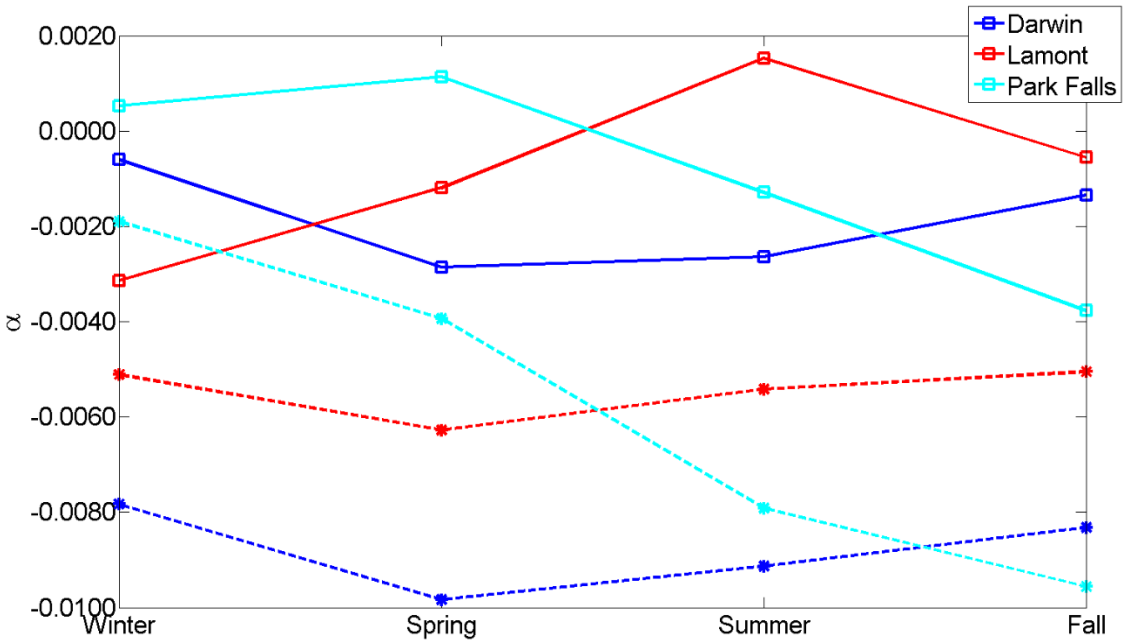

730

731 **Figure 9~~7~~: The average airmass-dependent correction factor for XCO_2 derived from a year of spectra**
732 **measured at Darwin, Lamont, and Park Falls for different seasons. The dashed lines with stars are the α for**
733 **XCO_2 retrieved using a Voigt line shape for both CO_2 and O_2 columns. The solid lines with squares are from**
734 **XCO_2 retrieved using the qSDV for both CO_2 and O_2 columns.**

735

736

737

738

739

740

741

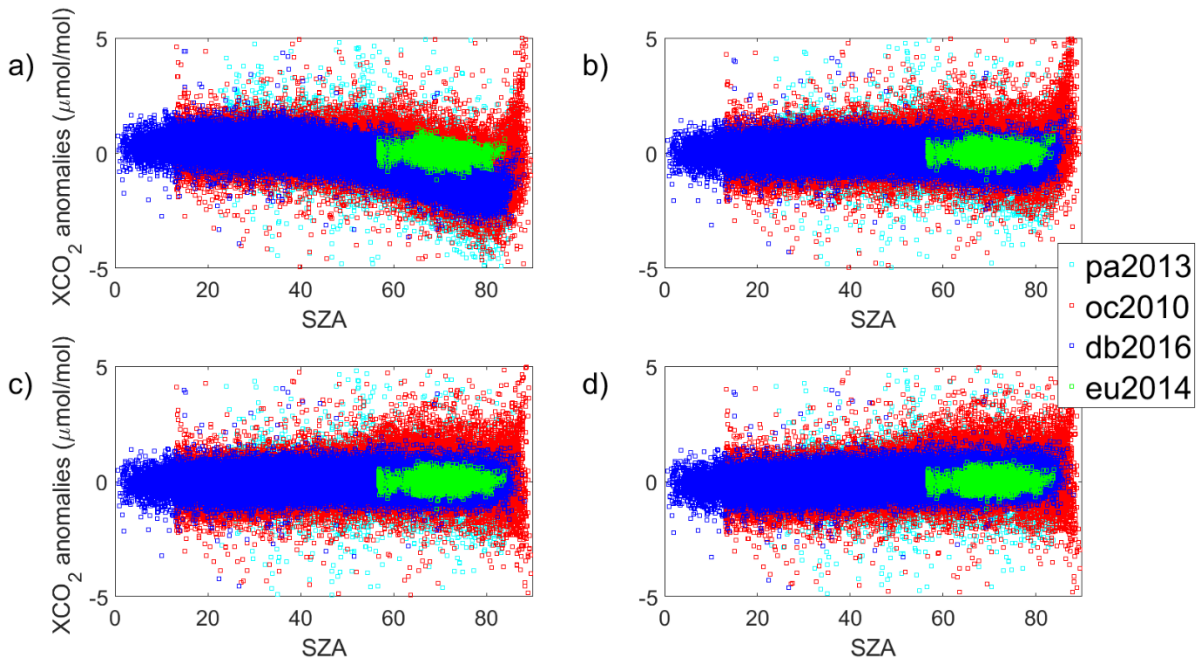

742

743 **Figure 108: (a) XCO_2 Voigt anomaly for a year of measurements from the four TCCON sites. The XCO_2**
744 **anomaly is the difference between each XCO_2 value and the daily median XCO_2. (b) The XCO_2 Voigt**
745 **anomaly after the airmass dependence correction is applied to the XCO_2 Voigt data. (c) XCO_2 qSDV**
746 **anomaly. (d) XCO_2 qSDV anomaly after correction for the airmass dependence.**

747

748

749

750

751

752

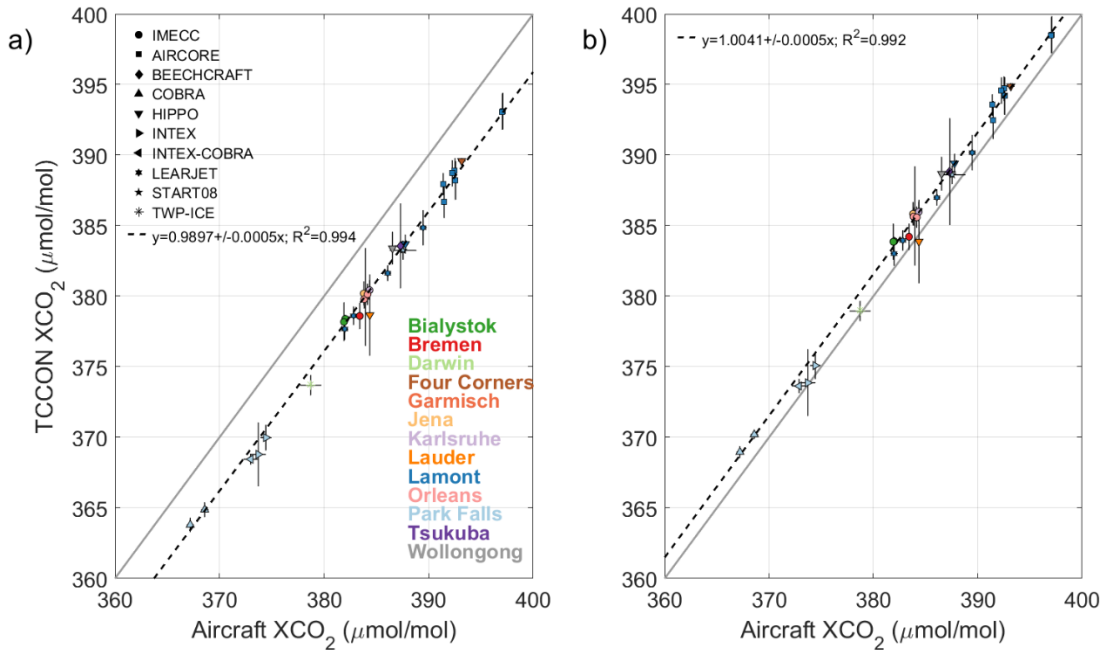

753

754 **Figure 119: (a) Correlation between TCCON and aircraft XCO_2 Voigt measurements for 13 TCCON sites.**
755 **Each aircraft type is indicated by a different symbol given by the legend in the top left corner. Each site is**
756 **represented by a different colour given by the legend in the bottom right corner. The grey line indicates the**
757 **one-to-one line and the dashed line is the line of best fit for the data. The slope of the line of best fit as well as**
758 **the error on the slope are given in the plot. (b) the same as (a) but for XCO_2 qSDV.**

759

760

761

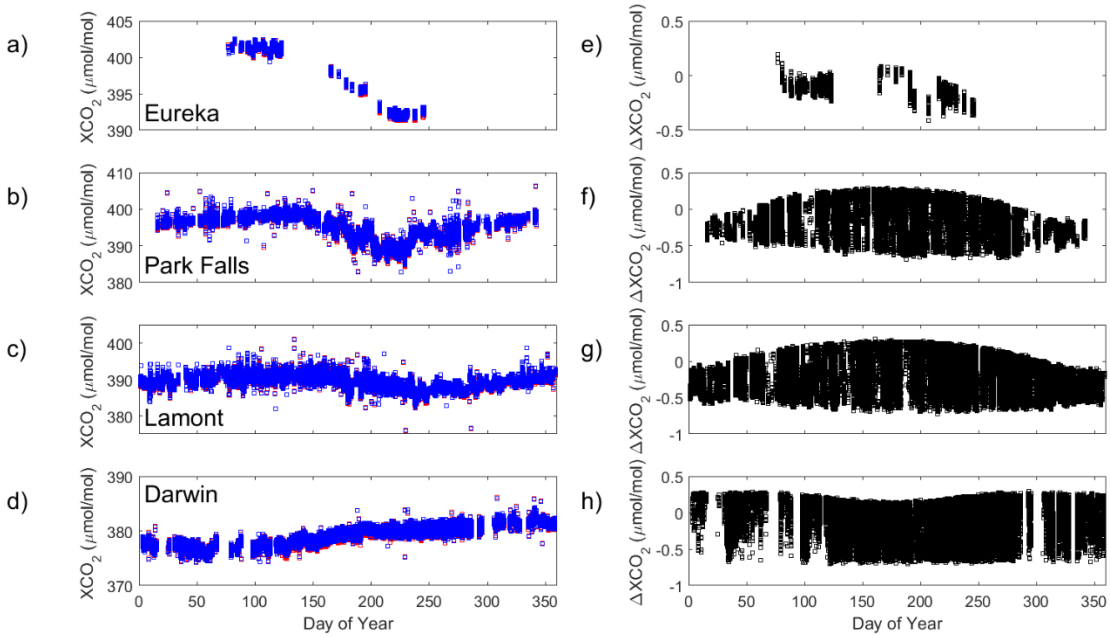

Figure 12~~10~~: (a) to (d) XCO_2 plotted as a function of day of the year for Eureka (2014), Park Falls (2013), Lamont (2010), and Darwin (2006) respectively. The mostly-hidden red boxes are XCO_2 calculated from using a Voigt line shape in the retrieval and the blue boxes are from using the qSDV. (e) to (h) the difference between XCO_2 Voigt and XCO_2 qSDV.

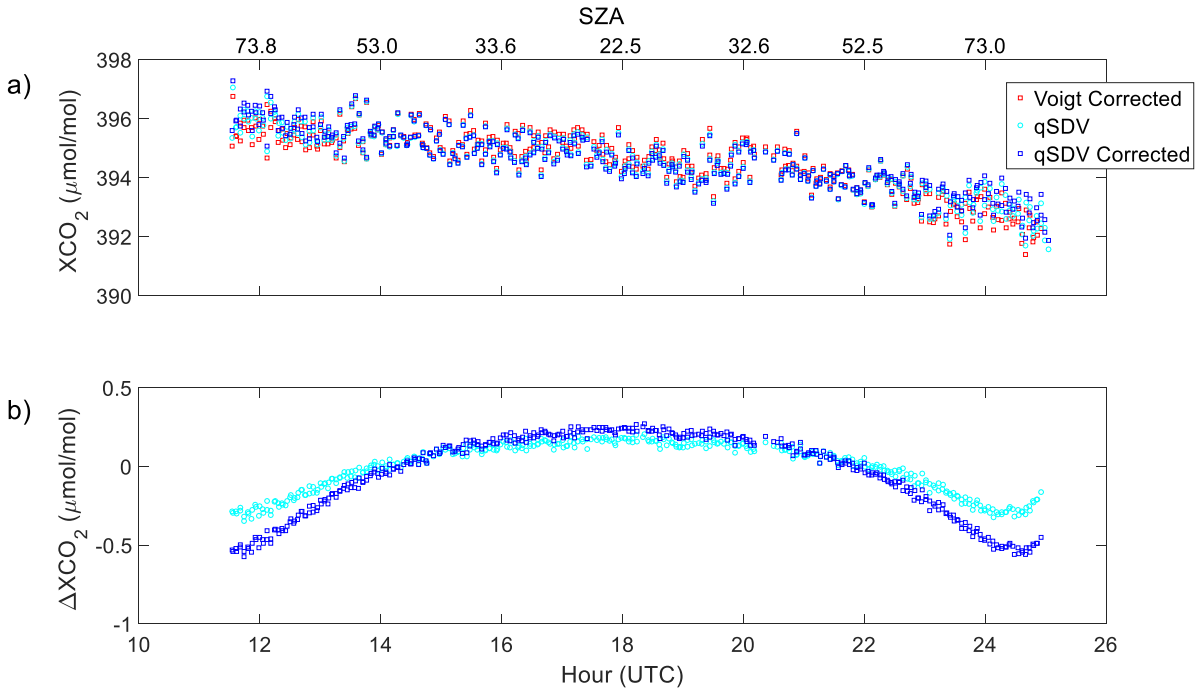

Figure 13~~11~~: (a) XCO_2 from Park Falls retrieved from spectra recorded on June 18, 2013. Plotted is XCO_2 retrieved: (1) with a Voigt line shape and corrected for the airmass dependence (red squares), (2) with the qSDV (cyan circles), and (3) with the qSDV and corrected for the airmass dependence (blue squares). (b) the difference between the Voigt XCO_2 corrected and the qSDV XCO_2 (cyan circles), and the difference between the Voigt XCO_2 corrected and the qSDV XCO_2 corrected (blue squares). The top x-axis is the SZA that corresponds to the hour on the bottom x-axis.